nature medicine

Article

https://doi.org/10.1038/s41591-025-04053-3

Immune profiling in a living human recipient of a gene-edited pig kidney

Received: 2 May 2025

Accepted: 9 October 2025

Guilherme T. Ribas[1], **André F. Cunha**[2], **Jonathan P. Avila**[3], **Alessia Giarraputo**[4], **Leela Morena**[1], **Karina Lima**[1], **Rodrigo B. Gassen**[1], **Jia-Yun Chen**[5], **Jia-Ren Lin**[5], **Sandro Santagata**[5,6], **Claire T. Avillach**[4], **Birgitta A. Ryback**[7], **Martin S. Lindner**[8], **Sivan Bercovici**[8], **Ivy A. Rosales**[4], **Tatsuo Kawai**[1], **Helder I. Nakaya**[3,9], **Robert B. Colvin**[4], **Thiago J. Borges**[1,10] ✉ & **Leonardo V. Riella**[1,10] ✉

Xenotransplantation of gene-edited pig kidneys offers a promising solution to the shortage of kidneys for organ transplantation. We recently performed a gene-edited pig kidney transplantation into a living human recipient with end-stage kidney disease. Here, using transcriptomics, proteomics, metabolomics and multiplexed imaging, we conducted high-dimensional immune profiling in this individual. Despite profound depletion of circulating T cells, early T cell-mediated rejection occurred within 1 week after transplantation, likely driven by subtherapeutic immunosuppression and the presence of residual $CD8^+$ T cells in lymph nodes. This T cell-mediated rejection event was reversed by intensified immunosuppression. After treatment, adaptive immunity remained suppressed, whereas innate immune activation, characterized by sustained monocyte and macrophage activity along with elevated levels of interleukin-1 beta and granulocyte–macrophage colony-stimulating factor, persisted. Comparative transcriptomic analysis showed that xenograft rejection profiles resembled those typically observed in human allograft rejection, while also revealing unique innate immune signatures. We did not detect antibody-mediated rejection. The levels of circulating pig donor-derived cell-free DNA rose during the initial rejection episode and declined with treatment, supporting the potential of cell-free DNA measurements as a noninvasive biomarker of xenograft rejection. These findings define the distinct immune landscape of kidney xenotransplantation and highlight the need for regimens targeting both innate and adaptive immunity to improve outcomes.

Chronic kidney disease affects approximately 25 million individuals in the USA, with many progressing to end-stage renal disease[1]. For these patients, kidney transplantation remains the gold standard treatment. However, the severe shortage of transplantable organs forces most patients to rely on dialysis. While dialysis is essential for maintaining fluid and electrolyte balance, it is associated with significant morbidity and mortality risks[2,3]. Alarmingly, more than half of the patients on the transplant waiting list will succumb to the disease within an average of 5 years[1]—a prognosis worse than many cancers—or become too ill to undergo transplantation by the time a kidney becomes available.

Xenotransplantation, the transplantation of organs from non-human species into humans, offers a promising solution to the critical organ shortage. If genetically engineered pig kidneys can demonstrate sustained safety and functional superiority over dialysis, they could provide a scalable and transformative alternative for the tens

A full list of affiliations appears at the end of the paper. ✉e-mail: tdejesusborges@mgh.harvard.edu; lriella@mgh.harvard.edu

of thousands of patients awaiting life-saving transplants. Advances in gene editing have enabled the development of pigs with enhanced immunological compatibility with human recipients[4]. These donor pigs, raised under stringent controlled conditions, provide kidneys similar in size and function to human organs while harboring genetic modifications designed to mitigate immune rejection.

On 16 March 2024, a historic milestone in transplantation was achieved at Massachusetts General Hospital with the xenotransplantation of a gene-edited pig kidney into a living human recipient[5]. In this groundbreaking procedure, a Yucatan pig kidney containing 69 genetic modifications (EGEN-2784) was successfully transplanted into a 62-year-old male patient. While nonhuman primate models have shown promising xenograft survival with optimized immunosuppressive regimens across different swine donors[4,6–9], the human immune system presents greater immunological challenges, including a high frequency of memory cells driven by prior vaccinations, diet and infections. As rejection remains an important obstacle, comprehensive characterization of immune responses following xenotransplantation is crucial for guiding future strategies.

The complexity of human immune responses is influenced by diverse factors such as genetic variability, age, chronic infections and environmental exposures. A comprehensive, multidimensional, longitudinal systems immunology approach is essential to uncover connections between biological pathways, the immunosuppression regimen and clinical outcomes. Here we employed different layers of biological information to systematically perform high-dimensional profiling of the evolving immune landscape in this human kidney xenotransplantation. By integrating longitudinal immune monitoring with transcriptomic and proteomic analyses, we aimed to unravel the complexities of human-xenograft interaction, define the immunological consequences, and identify key molecular pathways driving rejection and their correlation with clinical parameters. The findings provide critical insights into xenogeneic immune responses and have the potential to refine immunosuppressive strategies and possibly future porcine genetic edits, ultimately improving clinical outcomes in xenotransplantation.

Results

Temporal changes in the immune response following kidney xenotransplantation

To comprehensively assess the immune response triggered by kidney xenotransplantation, we characterized the recipient's immune profile using proteomics, metabolomics and clinical measurements (Fig. 1a). Using an unbiased, longitudinal, multilayered integrative approach, we identified three distinct immune clusters associated with xenotransplantation (Extended Data Fig. 1). Cluster analysis based on silhouette scores confirmed that three clusters provided the optimal separation (Supplementary Fig. 1): one cluster was defined by a progressive decline in analytes over time (Extended Data Fig. 1a), another showed an increase post-transplantation (Extended Data Fig. 1b) and the third displayed no clear temporal pattern (Extended Data Fig. 1c).

Focusing on the cluster of analytes that declined over time (Fig. 1b and Extended Data Fig. 1a), we hypothesized that the immunosuppressive regimen was a key driver of these changes. The regimen included rabbit antithymocyte globulin (ATG), rituximab (anti-CD20), high-dose steroids and an anti-C5 antibody (ravulizumab) as induction therapy, followed by maintenance immunosuppression with Fc-modified anti-CD154 monoclonal antibody (tegoprubart), tacrolimus, mycophenolic acid and prednisone (Extended Data Fig. 2). Network analysis with those declining features demonstrated that this cluster was enriched for pathways related to effector immune responses, cytokine-mediated signaling and T cell proliferation and activation (Fig. 1c). Notably, when investigating individual features, we found that several downregulated proteins corresponded to specific effects of immunosuppressive drugs, including CD19 (rituximab), CD8A and CD4 (ATG), interleukin-2 RA (IL-2RA) (tacrolimus and mycophenolic acid), GZMB and tumor necrosis factor (TNF) (steroids, tacrolimus and mycophenolic acid), CD80 (mycophenolic acid), ITGAM and CXCL9/10 (tegoprubart) (Fig. 1d). CD19 was selected over CD20 as a marker of B cell depletion because it is more broadly expressed across B cell subsets and remains a stable and reliable surrogate following rituximab treatment, whereas CD20 expression can be variably affected by antibody binding.

This immune modulation was associated with improved graft function, reflected by declining creatinine and cystatin C levels. Additional laboratory trends, including reductions in glucose and magnesium and a fluctuating lactate dehydrogenase pattern, were also observed (Fig. 1e), though these are influenced by multiple factors beyond allograft status. Several T cell-associated metabolites, such as homocysteine[10], caproic acid[11] and oxoglutaric acid[12], also showed substantial reductions following xenotransplantation (Fig. 1c). In addition, we observed a decrease in indoxyl, a metabolite linked to chronic kidney disease[13,14] and end-stage renal disease[15], correlating with improved kidney function observed in our xenotransplant recipient[5]. Together, these findings demonstrate a striking shift in the circulating immune composition following xenotransplantation, consistent with the selective targeting of adaptive immunity by the immunosuppressive regimen.

Longitudinal single-cell RNA sequencing analysis of peripheral blood mononuclear cells in xenotransplantation

We performed single-cell RNA sequencing (scRNA-seq) on peripheral blood mononuclear cells (PBMCs) collected at six time points to gain a high-resolution view of the systemic cellular immune dynamics. After quality filtering, approximately 36,000 high-quality cells were analyzed. To better identify the immune subsets, we integrated the longitudinal recipient samples with 22 external healthy control samples from public PBMC datasets. Integrative analysis identified 17 unsupervised distinct cell clusters based on their transcriptomic profiles (Fig. 2a). Using Louvain clustering, we annotated PBMC subsets and mapped their dynamic proportions over time (Fig. 2a and Extended Data Fig. 3). Integration of longitudinal scRNA-seq data into a temporal UMAP embedding revealed a progressive decline in adaptive immune cells, accompanied by an increase in innate immune cells observed at all post-transplant time points relative to baseline (Fig. 2b). Specifically, $CD4^+$ and $CD8^+$ T cells, B cells and regulatory T (T_{reg}) cells exhibited a profound reduction compared to pretransplant (Fig. 2c). A xeno-crossmatch assay, incubating the recipient's serum with donor pig PBMCs, detected no xenoantibodies (Extended Data Fig. 4), consistent with B cell depletion and ongoing blockade of CD40–CD40L costimulation.

In contrast to adaptive immune cells, innate myeloid populations, including $CD14^+$ and $CD16^+$ monocytes and conventional dendritic cells, were proportionally increased over time relative to pretransplant (Fig. 2c). A detailed characterization of monocyte subsets revealed distinct gene expression profiles over time, using the pretransplant time point as baseline. We identified three major gene expression patterns: gene set 1 (red) included genes upregulated after transplantation; gene set 2 (green) comprised genes that were downregulated; and gene set 3 (purple) contained genes predominantly expressed by $CD16^+$ monocytes (Extended Data Fig. 5). Most differentially expressed genes were associated with the migration and differentiation of circulating monocytes into peripheral tissues, including *DDIT4*[16], *IL1R2*[17], *C1QB*[18], *CX3CR1*[19], *DUSP5*[20] and *EGR1*[21].

Flow cytometry validated the scRNA-seq findings, revealing a pronounced decrease in $CD4^+$ and $CD8^+$ T cells, T_{reg} cells and B cells (Fig. 2d and Supplementary Fig. 2), along with a relative expansion of $CD14^+$ monocytes and conventional dendritic cells compared to pretransplant levels (Fig. 2d). These findings indicate a profound shift in the systemic immune landscape, characterized by a suppression of adaptive immunity and the emergence of an innate immune signature.

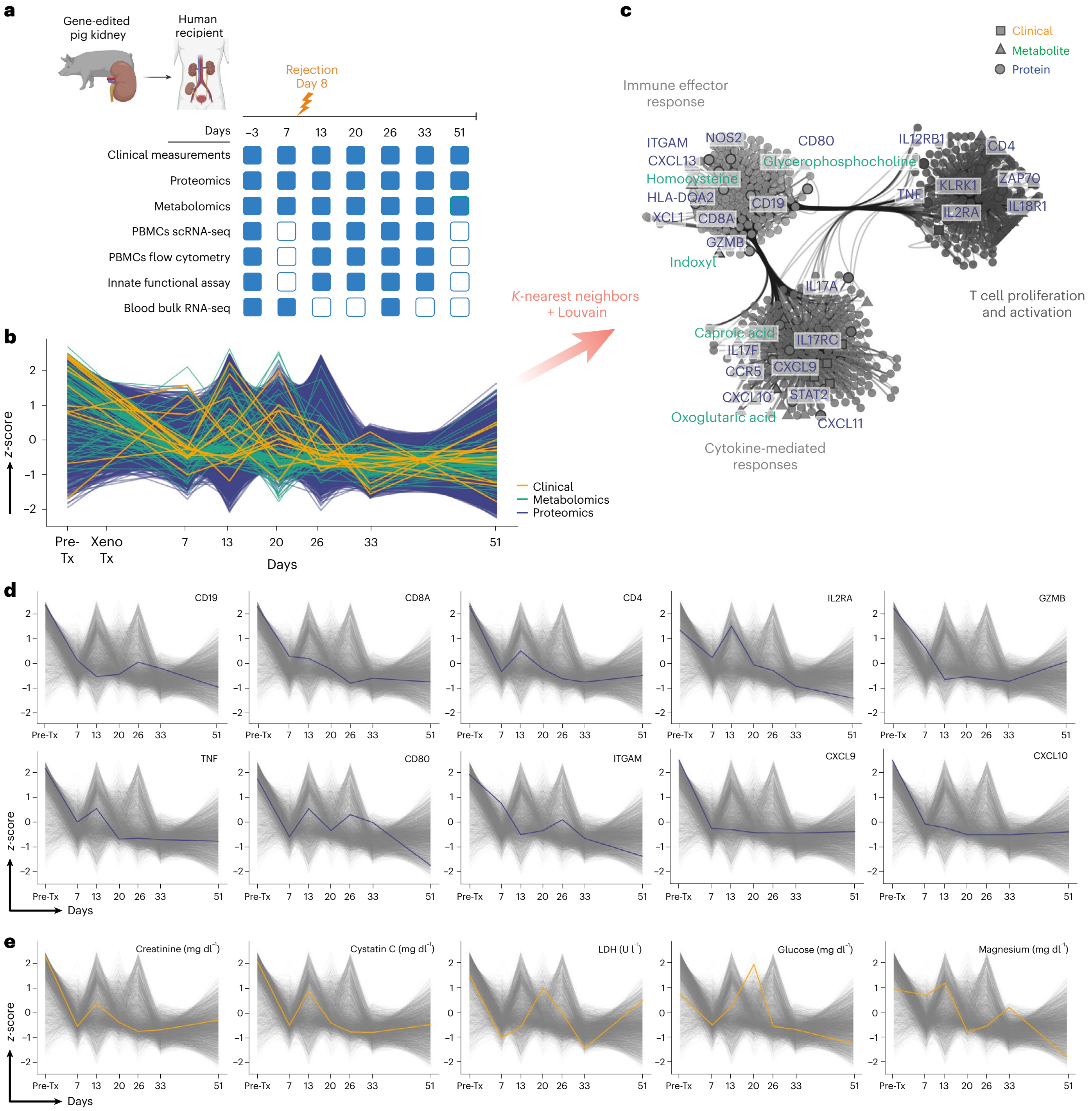

Fig. 1 | Immunosuppression suppresses the adaptive immune response following xenotransplantation. a, Research protocol and sample collection schedule. **b**, Integrative clustering of proteomics, metabolomics and clinical parameters using Fuzzy C-Means clustering across all time points. **c**, Network analysis integrating proteomics, metabolomics and clinical data, highlighting modules associated with immune-effector responses, cytokine-mediated responses and T cell proliferation and activation. **d**, Longitudinal measurements of circulating protein levels impacted by the immunosuppression regimen. The blue line represents the normalized levels (*z*-score) of the indicated circulating protein at different times. **e**, Longitudinal measurements of clinical biomarkers, including creatinine, cystatin C, lactate dehydrogenase, glucose and magnesium. The orange line represents the normalized levels (*z*-scored) of the indicated clinical measurements at different times. Pre-Tx, pre-transplantation.

Persistent innate immune responses post-xenotransplantation

The second immune cluster identified through multi-omics analysis consisted of analytes that increased following xenotransplantation (Fig. 3a). This cluster was enriched for pathways associated with innate immune activation, including the Toll-like receptor 4 cascade, IL-1 signaling and Fc-receptor signaling (Fig. 3b). Key signaling molecules within these pathways, such as BIRC2, MAPK8, MAP2K3, IKBKB and IKBKG were upregulated (Fig. 3b). Moreover, levels of inflammatory metabolites, including L-kynurenine[22] and eicosenoic acid[23], also increased following xenotransplantation (Fig. 3b).

https://doi.org/10.1038/s41591-025-04053-3

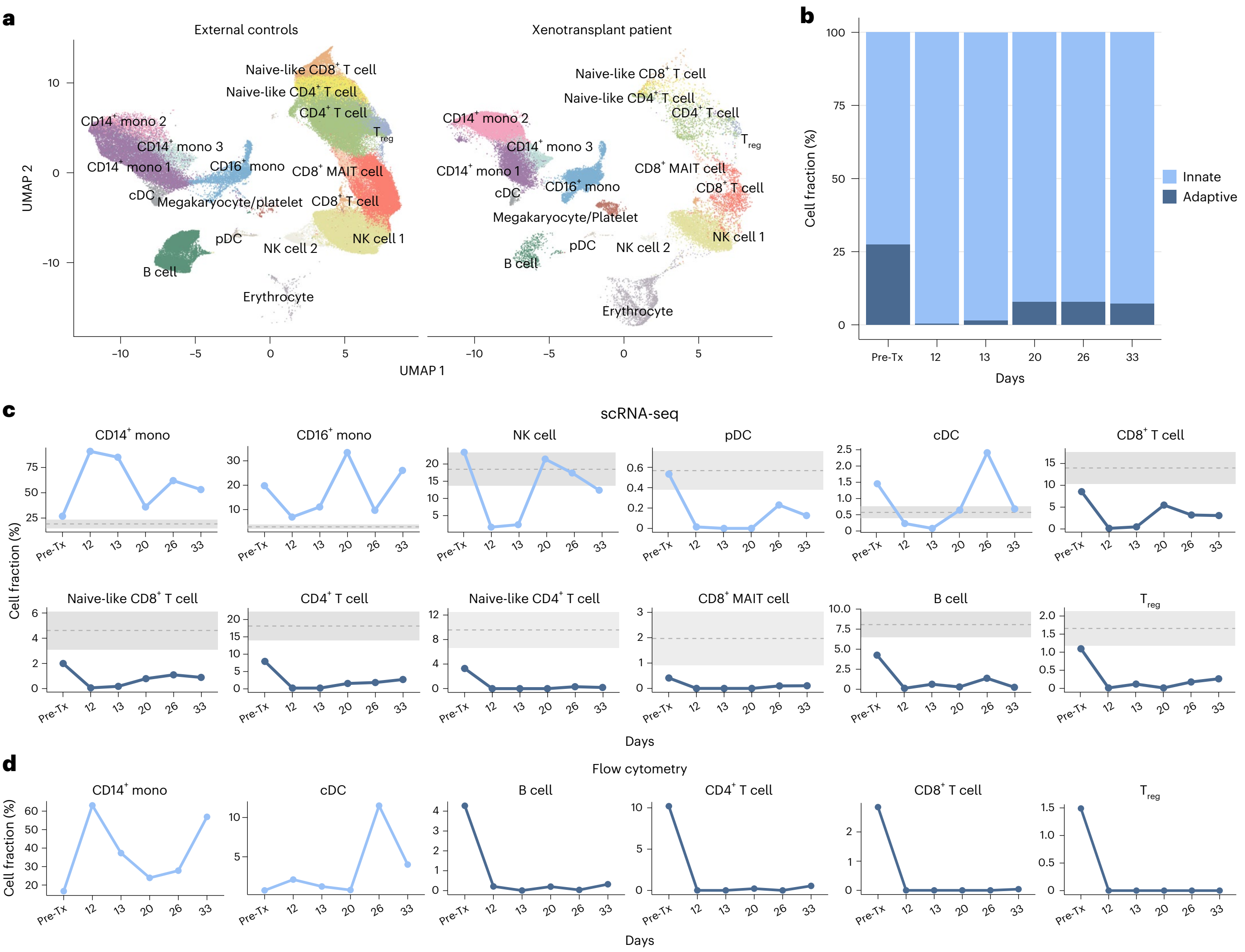

Fig. 2 | Single-cell RNA sequencing analysis of peripheral immune cells following xenotransplantation. a, UMAP plot illustrating the PBMC subsets identified by scRNA-seq. Data obtained from longitudinal PBMC samples from the recipient were integrated with data from 22 healthy control samples from publicly available datasets (GSE165080 (ref. 39), GSE171555 (ref. 40) and GSE192391 (ref. 41)). **b**, Proportions of innate and adaptive immune cells in PBMC samples over time. **c**, The proportion (percentages) of PBMC subsets, derived from single-cell RNA-seq, at the indicated time points. Dashed lines indicate the mean proportions of cells for each cell type in the external control group, with the shaded areas indicating the 95% confidence interval around the mean. Cell fractions were calculated excluding erythrocytes and megakaryocytes/platelets. **d**, Circulating immune cell subsets, as quantified by flow cytometry at the indicated time points. Cell fractions represent percentages of viable lymphocytes. See also Supplementary Fig. 2 for gating strategies related to the flow cytometry analysis. cDC, conventional dendritic cell; pDC, plasmacytoid dendritic cell.

To further investigate the functional implications of these findings, we measured cytokine production in response to innate immune stimulation (Fig. 3c). From analysis of 65 cytokines, we detected increases in IL-1β (Fig. 3d), IL-6 (Fig. 3e), IL-8 (Fig. 3f) and granulocyte–macrophage colony-stimulating factor (GM-CSF) (Fig. 3g) following PBMC stimulation with toll-like receptor (TLR) ligands. This cytokine surge paralleled the expansion of monocytes and conventional dendritic cells, suggesting heightened TLR and NF-κB signaling post-xenotransplantation. Furthermore, we identified an increase in type I interferon-related molecules, including IRF5, TIRAP and ISG15, as well as the metabolite adenine[24] (Fig. 3b). Taken together, these findings indicate that despite potent immunosuppression targeting adaptive immunity, innate immune activation persists and is augmented over time, highlighting the need for tailored immunosuppressive regimens and/or additional gene editing strategies that mitigate the innate immune responses in xenotransplantation.

Tissue transcriptional signatures during xenograft rejection

Within the first week post-transplant, the recipient developed a Banff grade 2A T cell-mediated rejection (TCMR), confirmed by a biopsy on day 8. This rejection occurred despite a marked reduction in circulating adaptive immune cells, shown by our longitudinal scRNA-seq and flow cytometry analyses. Examination of T cell depletion in secondary lymphoid organs revealed that while T cells were effectively depleted from circulation at the time of transplant, persistent CD8$^+$ T cells were still detected on draining lymph nodes (Extended Data Fig. 6). These findings suggest that circulating immune cell counts may not fully reflect the extent of depletion or the risk of rejection. We reasoned that the presence of activated T cell populations that were primed in the secondary lymphoid organs and then migrated to the graft likely contributed to the early rejection episode. However, this hypothesis requires formal investigation.

To manage the rejection, the recipient was treated with two pulses of glucocorticoids, anti-IL-6R monoclonal antibody therapy on day 8,

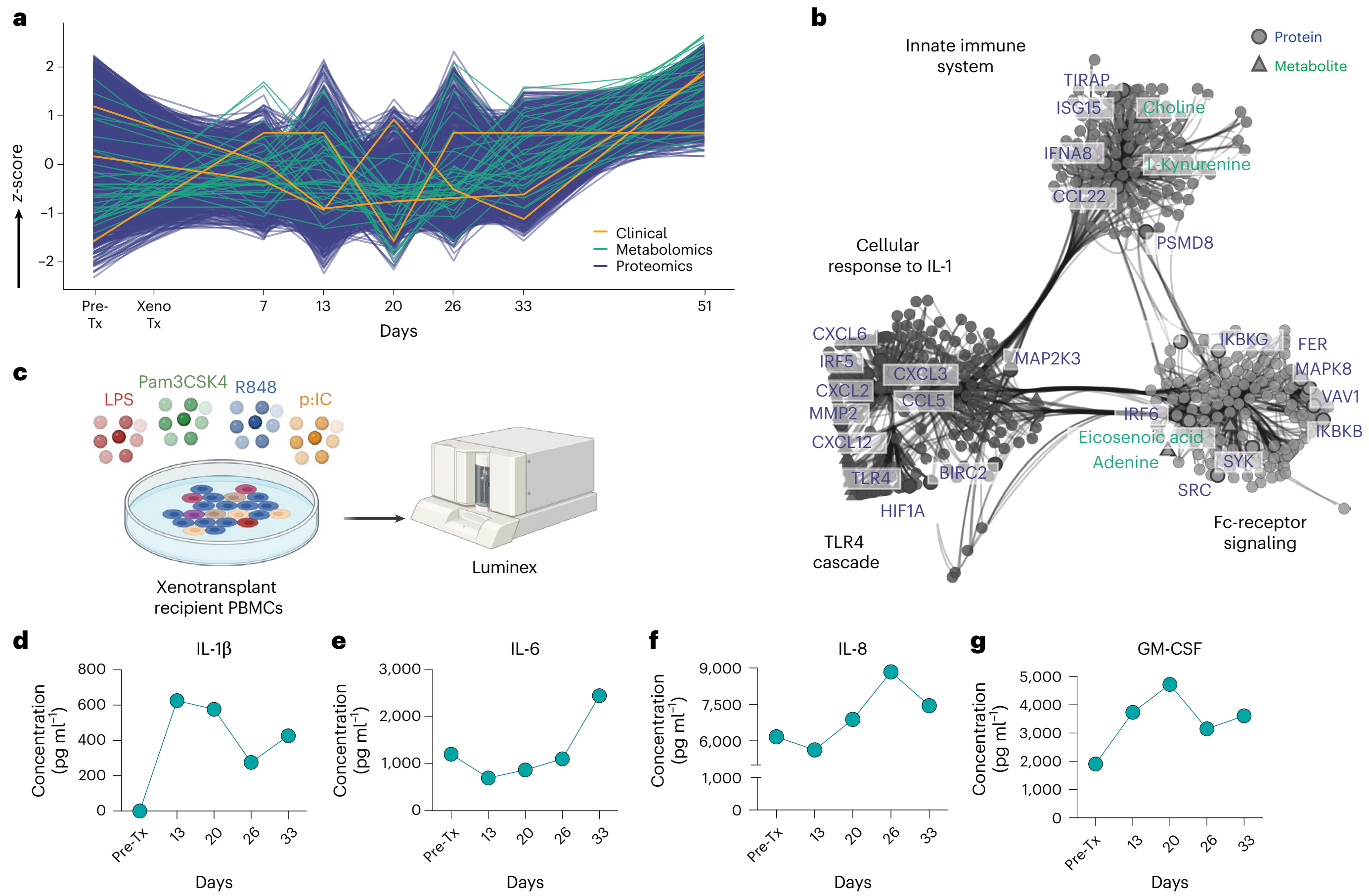

Fig. 3 | Innate immune activation increases after xenotransplantation. **a**, Integrative clustering of clinical, proteomic and metabolomic data using Fuzzy C-Means clustering across all time points. Normalized multi-omics revealed analytes that increased after xenotransplant despite the administered immunosuppressive regimen. **b**, Network analysis integrating proteomic and metabolomic data shows several modules enriched for innate immunity pathways. **c**, Experimental scheme showing that recipient PBMCs obtained at multiple time points were stimulated for 24 h with a regimen of TLR ligands (LPS, Pam3CSK4, R848 and p:IC), following which cytokine concentrations were measured in supernatants using a Luminex device. **d**–**g**, Longitudinal concentrations of IL-1β (**d**), IL-6 (**e**), IL-8 (**f**) and GM-CSF (**g**) following TLR ligand stimulation.

and T cell depletion with ATG on days 9 and 10, along with an increased dosage of tacrolimus and mycophenolic acid (Fig. 4a). Due to C3 deposition observed in the biopsy sample[5], the C3 inhibitor pegcetacoplan was administered from day 12 to day 28.

We performed bulk mRNA analysis using the NanoString nCounter platform to assess molecular immune changes associated with rejection. Transcriptional profiles from the rejection biopsy (day 8) were compared to those from a stable, nonrejection (nonR) time point (day 34) and the contralateral kidney of the donor pig (donor, day 0) (Fig. 4b). Representative hematoxylin and eosin stains of the kidney xenograft biopsies are shown in Fig. 4c. We compared these findings with transcriptomic data from archival human kidney allograft biopsies described in ref. 25, which included 15 samples from living donor biopsies, 84 from stable time points post-transplant, 36 from TCMR and 89 from chronic active antibody-mediated rejection (CAMR). Compared to the day 0 biopsy, xenograft rejection was associated with increased expression of both adaptive and innate immune transcripts. Adaptive immunity markers included elevated CD4$^+$ (Fig. 4d) and CD8$^+$ T cell signatures (Fig. 4e). Innate immune responses were characterized by increased natural killer (NK) cells (Fig. 4f), M1 (Fig. 4g) and M2 macrophages (Fig. 4h) and TLR signaling (Fig. 4i). These immune signatures closely resembled those observed in human kidney allograft TCMR and were partially resolved at the subsequent nonR time point (day 34, Fig. 4d–i). In addition, the rejection biopsy also showed transcriptomic evidence of activation of other pathways, including adaptive immunity, IL-12 family signaling, cytokine signaling, innate immune system, type I interferon signaling, MHC class I antigen presentation, cytosolic DNA sensing, NOTCH signaling and programmed cell death. The levels of these pathways were comparable to or higher than those seen in human allograft TCMR samples (Extended Data Fig. 7a–i). Our data demonstrate that xenograft rejection shares key molecular features with human allograft rejection, including adaptive and innate immune activation within the tissue microenvironment.

Multiplexed imaging reveals the cellular landscape of xenograft rejection

To complement transcriptomic profiling and provide spatial resolution of the immune infiltration, we performed multiplexed tissue immunofluorescence to characterize the cellular landscape of xenograft rejection. Kidney tissues from day 0 (donor), day 8 (TCMR) and day 34 (stable, nonR) post-transplantation were stained for glomerular and tubular markers (podocin and β-catenin), total leukocytes (CD45), endothelial cells (CD31), T lymphocytes (CD4 and CD8), macrophages (CD68 and CD163) and NK cells (NKG2A). Compared to the day 0 biopsy, rejection was marked by severe interstitial inflammation and mild glomerulitis (Fig. 5a). The immune infiltrate was characterized by increased CD4$^+$ and CD8$^+$ T cells, M1 (CD68$^+$) and M2 (CD163$^+$) macrophages, and NK cells (Fig. 5a,b). CD4$^+$ T cells and CD68$^+$ macrophages were the most prominently upregulated subsets during rejection (Fig. 5a,b). Notably,

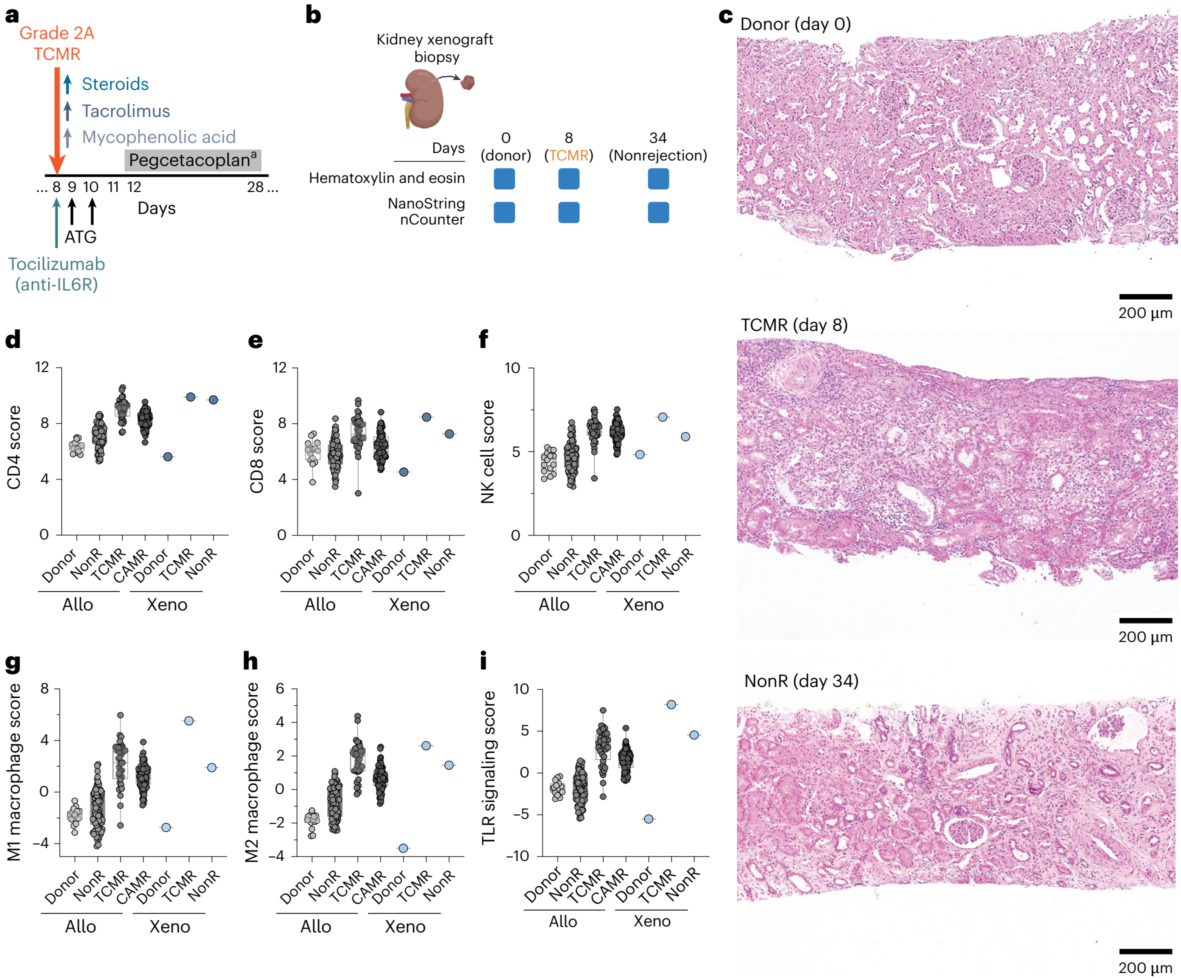

Fig. 4 | Tissue transcriptional profiling reveals upregulation of innate and adaptive transcripts during xenograft rejection. a, An illustration of the immunosuppressive regimen used to treat the recipient who experienced a TCMR, categorized as grade 2A according to Banff criteria, on day 8 post-xenotransplantation. **b**, Research protocol and the schedule for kidney biopsy collection. **c**, Hematoxylin and eosin staining of kidney xenograft biopsies at the indicated time points. **d**–**i**, Kidney xenograft biopsies were analyzed using the NanoString nCounter platform. Findings were compared to transcriptomic profiles from archival human kidney allograft biopsies[25], including 15 living donor samples, 84 stable post-transplant time points, 36 cases of TCMR and 89 cases of CAMR. We compared cell-type-specific and immune-signaling-specific transcriptional signatures including CD4 T cells (**d**), CD8 T cells (**e**), NK cells (**f**), M1 macrophages (**g**), M2 macrophages (**h**) and TLR signaling (**i**). Allo, allogeneic donor, $n = 15$ samples; nonR, $n = 84$ samples; TCMR, $n = 36$ samples; CAMR, $n = 89$ samples. In **d**–**i**, data are represented as box plots with the center line representing the median, and the box limits are the minimum and maximum quartiles. All data points are displayed. [a]C3 inhibitor.

while T cells, M1 macrophages and NK cells declined after rejection treatment, M2 macrophages remained persistently elevated in the xenograft microenvironment (Fig. 5b). Human-specific HLA class I staining indicated that the majority of macrophages were of human origin (Extended Data Fig. 8), reflecting heightened innate immune activity. These spatial findings corroborate transcriptomic data, confirming that xenograft rejection is driven by coordinated infiltration of T cells and macrophages, mirroring patterns observed in human allograft rejection. Persistent M2 macrophage presence post-treatment highlights potentially ongoing innate immune activity within the graft.

Peripheral transcriptional and proteomic profiles of xenograft rejection

To determine whether immune events within the graft were reflected systemically, we assessed correlations between tissue immune activation and circulating immune cell dynamics. Since PBMCs were unavailable on the day of rejection (Fig. 1a), we inferred immune cell subsets from bulk RNA-seq data using the CIBERSORT tool (Fig. 6a). Consistent with the tissue findings, we observed increased proportions of CD4$^+$ T effector memory (TEM) cells, CD16$^+$ monocytes and CD14$^+$ monocytes on day 8 compared to pretransplant (Fig. 6b). While CD4$^+$ TEM cells and total monocytes declined following rejection treatment, the subset of CD14$^+$ monocytes remained persistently elevated. This continuous elevation may reflect ongoing innate immune activity associated with tissue repair or subclinical inflammation, underscoring the need for further studies to clarify their role in postrejection graft outcomes.

To investigate broader systemic immune changes, we compared peripheral blood gene and protein expression profiles during rejection (day 7) and at a stable, nonR time point (day 26). This analysis identified 207 differentially expressed genes and proteins, including 181 upregulated and 26 downregulated targets (Fig. 6c). Upregulated signatures were enriched in pathways related to myeloid cell signaling, IL-6 and IL-12 signaling, and effector T cell activation (Fig. 6c). Key upregulated targets included CXCL10, STAT1, STAT3, CD163 and NLRP3 (Fig. 6d). Downregulated pathways were related to glycosylation (Fig. 6c), with reduced expression of B3GAT1, B4GAT1 and ST6GALNAC4 (Fig. 6d). These findings indicate that xenograft rejection is associated with coordinated transcriptional and proteomic changes involving both adaptive and innate immune activation, detectable in the peripheral blood.

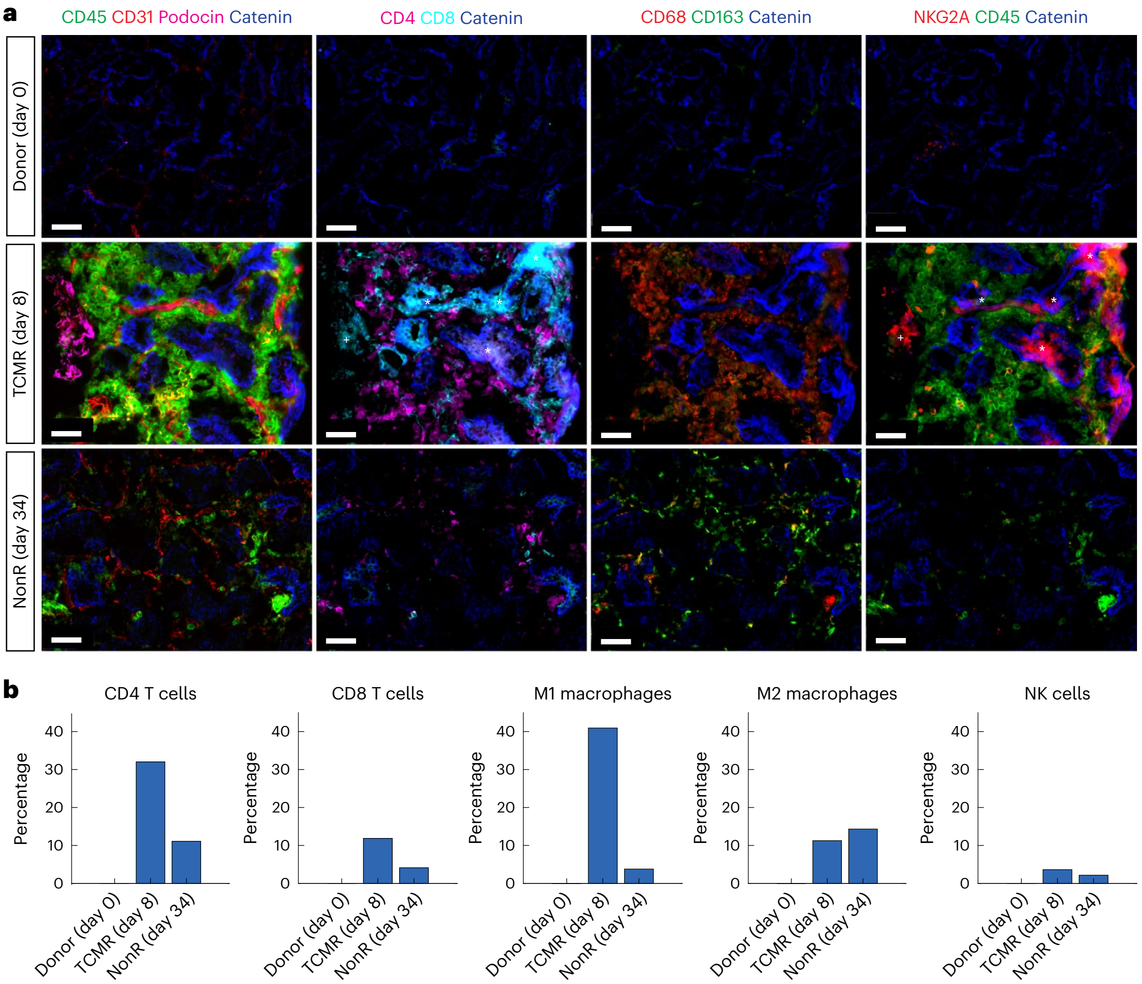

Fig. 5 | Multiplexed immunofluorescence reveals increased T cells and CD68$^+$ macrophages during xenograft rejection. a, Representative multiplexed immunofluorescence images of kidney biopsies from the donor pig (day 0) and xenograft tissues on post-transplant days 8 (TCMR) and 34 (nonR). Images were acquired from equivalent regions on each slide using distinct channel combinations. Podocin marks glomeruli (podocytes); β-catenin marks tubular epithelium. Background staining of CD8 and NKG2A in tubular and glomerular regions is indicated by + (glomerulus) and * (tubule), respectively. Scale bars, 50 μm. **b**, Quantification of immune cell subsets (percentage of total cells) across whole-slide sections from donor, TCMR and nonR xenotransplant biopsy samples from **a**. Gating strategies are detailed in Methods. Quantification was independently repeated twice with similar results.

In addition to immune cell and transcriptomic profiling, we assessed whether levels of porcine donor-derived cell-free DNA (dd-cfDNA), a circulating marker of tissue damage widely used in allotransplantation[26], correlated with graft injury in the xenotransplantation setting. We tracked both porcine-derived cfDNA and recipient-derived human cfDNA. At the time of rejection, porcine dd-cfDNA levels increased markedly (~1,000-fold by day 9), indicating xenograft injury (Fig. 6e). A modest, delayed rise (~10-fold) in human cfDNA was also observed, potentially reflecting recipient immune cell turnover associated with rejection and immunosuppressive treatment, including T cell depletion. Following treatment, porcine dd-cfDNA levels declined substantially, consistent with histological resolution of the immune response and restoration of graft stability (Fig. 6e). These findings suggest that species-specific cfDNA may serve as a dynamic noninvasive biomarker for early detection and monitoring of xenograft injury.

Lastly, we investigated whether the blood transcriptional profile observed during xenograft rejection in kidney xenograft recipients resembled those observed in human kidney allograft rejection. Using the publicly available dataset GSE120649 (ref. 27) from human kidney transplant recipients, we compared blood transcriptomics from our xenograft recipient with a previously described transcriptional rejection signature of human allograft rejection[28]. Distance correlation analysis, which captures nonlinear relationships, revealed that the xenograft rejection sample (day 7) clustered with human kidney allograft rejection profiles, while the nonrejection sample (day 26) aligned with human nonrejection states (Fig. 6f). These results demonstrate significant molecular overlap between xenograft and allograft rejection in both tissue and peripheral blood, suggesting conserved immune pathways that could guide future strategies for immune monitoring and therapeutic intervention in xenotransplantation.

Discussion

Here we report the high-dimensional immune characterization of a gene-edited pig kidney xenotransplantation in a living human. Using longitudinal transcriptomic, proteomic analyses and spatial analyses, we observed a profound shift in adaptive immunity, while innate immune activation persisted despite immunosuppression. The recipient experienced a TCMR episode within the first week post-transplant, marked by the presence of T cells and macrophages in the tissue, which improved following treatment. This study provides critical insights into xenogeneic immune responses, highlighting the need to optimize immunosuppressive strategies and potentially guide future porcine donor gene editing to improve clinical outcomes in xenotransplantation.

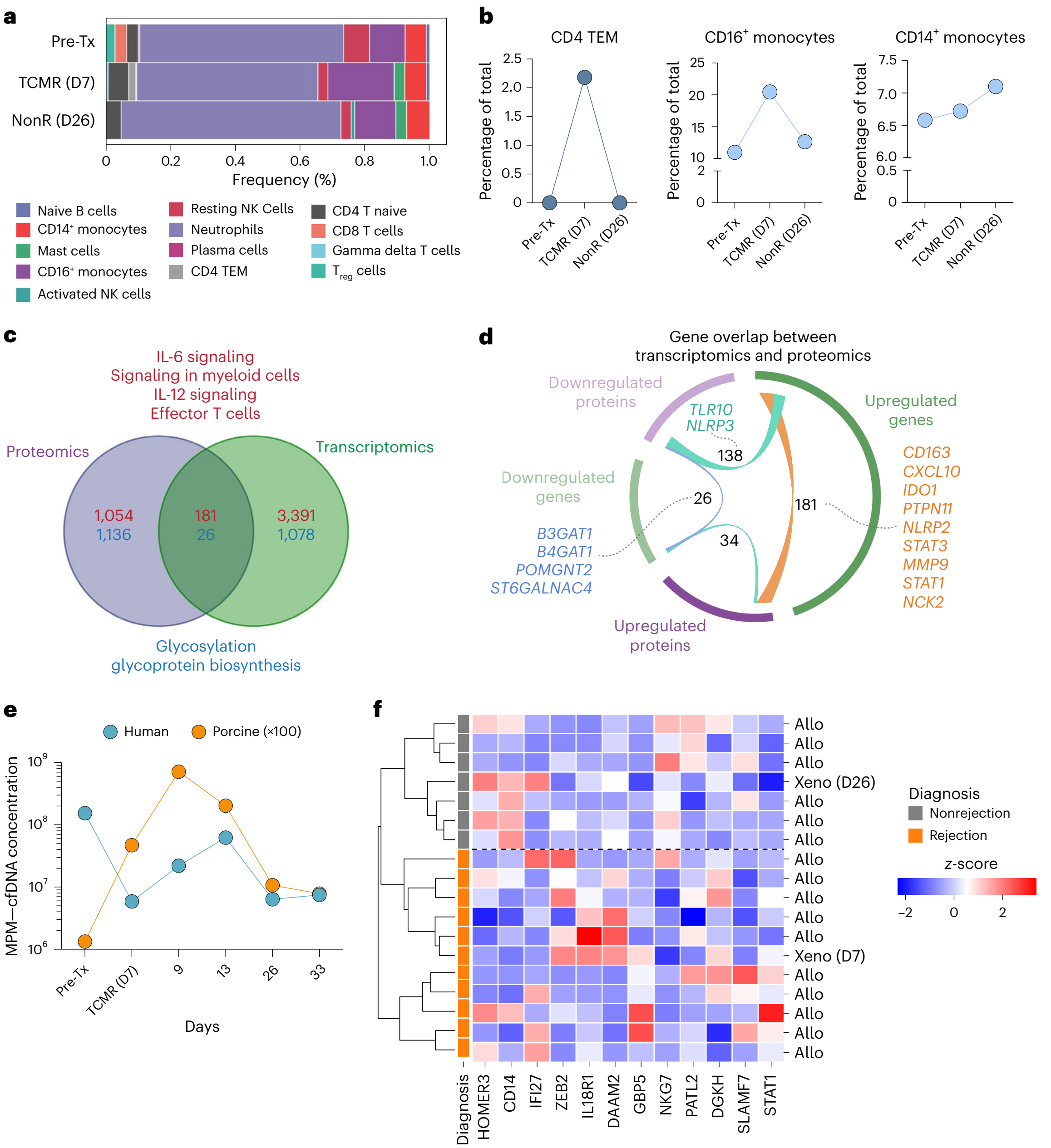

Fig. 6 | Peripheral proteomic and transcriptomic signatures, cfDNA dynamics and comparison with human allograft rejection. **a**, Circulating immune cell proportions inferred from blood bulk transcriptomics data using CIBERSORT at Pre-Tx, during TCMR (day 7) and at a stable, nonR time point (day 26). **b**, Longitudinal changes in CD4 TEM cells, CD16$^+$ monocytes and CD14$^+$ monocytes. **c**, Pathways enrichment analysis of transcriptomics and proteomics datasets. Numbers in red indicate pathways enriched for upregulated genes and proteins. Numbers in blue indicate pathways enriched for downregulated genes and proteins. **d**, Overlap between differentially expressed genes and proteins in peripheral blood at rejection (day 7) versus nonR (day 26) time points. Green bars represent genes; purple bars represent proteins. Links indicate overlapping features, with dashed lines highlighting shared genes. **e**, Longitudinal concentrations of host-derived and pig-derived cfDNA; MPM, molecules of host-derived or pig-derived cfDNA per µl of plasma. **f**, Expression of a peripheral blood transcriptional signature associated with human allograft rejection across xenograft and allograft samples (human allograft rejection, $n = 10$; nonR, $n = 6$; data were obtained from GSE120649). The dashed line highlights the separation between rejection and nonR clusters.

We identified key differences in immune dynamics between our kidney xenograft patient, xenotransplantation in decedent recipients and human allograft rejection, particularly regarding the type and timing of rejection. Potential factors contributing to the observed differences include variability in donor animals, patient selection criteria, immunosuppressive regimens, baseline inflammation and immune alterations associated with brain-dead donors. Our xeno recipient developed TCMR within 1 week of transplant, which is a rare occurrence in human allotransplantation when T cell depletion with thymoglobulin is used. However, a reduced dose of ATG (1.5 mg kg^{-1} versus standard 4.5 mg kg^{-1}) was administered in our case due to significant lymphopenia and hypersensitivity reaction after the first ATG dose[29]. TCMR was absent in most reports using decedent models[30,31], except for one group that used a low-dose ATG induction therapy (~2.5 mg kg^{-1}) and reported a mixed TCMR and antibody-mediated rejection[32]. Despite differences in timing, the xenograft biopsy profile resembled human allograft rejection, with prominent T cells and macrophages, and transcriptional upregulation of IFNγ, IL-1 and IL-6 signaling pathways[25]. The rejection episode was successfully treated with standard immunosuppressants, indicating that xenograft TCMR responds to conventional rejection therapies. However, xenograft rejection also showed distinct peripheral blood features, including heightened innate immune activation involving TLR signaling and type I interferon pathways. These findings suggest that xenograft rejection engages unique immune mechanisms that may require tailored therapeutic interventions, and greater T cell depletion might be needed to prevent TCMR.

In nonhuman primate (NHP) and human decedent xenotransplantation models, circulating B cells were detected post-xenotransplant[31] and antibody-mediated rejection (AMR) was typically the dominant rejection mechanism rather than TCMR[4,30,33]. By contrast, our patient showed no histological or serological evidence of AMR, likely due to effective pretransplant B cell depletion and ongoing CD154 costimulation blockade. Our observation of a lack of AMR compared to preclinical primate models may be explained by species-specific differences in humoral immunity and drug efficacy. Human IgM natural antibody binding to 3KO pig cells is significantly lower than that observed in Old World monkeys[34], and human transgenes introduced in 3KO pigs may function more effectively in humans than in NHPs. In addition, the greater cross-reactivity of clinical immunosuppressive agents in humans may contribute to improved control of AMR in our clinical setting, despite the use of similar immunosuppressive regimens. However, persistent CD8$^+$ T cells in lymph nodes highlight residual cellular immunity. Peripheral blood monitoring failed to detect early rejection, whereas porcine dd-cfDNA levels correlated with graft injury, suggesting species-specific cfDNA as a promising noninvasive biomarker. These findings emphasize the need for improved monitoring tools, such as dd-cfDNA assays and advanced imaging, to detect rejection before clinical dysfunction.

We observed persistent innate immune activation despite effective suppression of the adaptive immune response. This was characterized by a sustained increase in monocyte and macrophage populations, upregulation of TLR/NF-κB signaling and type I interferon responses, and elevated proinflammatory cytokine levels following TLR stimulation. This is corroborated by observations in decedent models showing human innate immune cells rapidly infiltrate pig xenografts following transplantation[30,31,35]. Similar systemic inflammation has also been reported in NHP xenotransplantation models[36], and it may have contributed to the early onset of TCMR post-xenotransplantation in our patient. Potential drivers of this innate immune response include xenograft-derived damage-associated molecular patterns, which stimulate monocytes and macrophages, and incomplete immune regulation by current immunosuppressive strategies. Existing therapies primarily target T and B cells while largely neglecting innate immune pathways. Although our xenotransplant recipient developed a fatal cardiac event on day 51, no acute myocardial infarction was found on autopsy[5]. Rather, chronic myocardial fibrosis, likely related to prior microvascular disease from prolonged dialysis, was identified and may have predisposed the patient to arrhythmia. Further studies are warranted to evaluate the potential contribution of xenograft-associated systemic inflammation to cardiovascular risk.

Notably, M2 macrophages remained elevated in the xenograft microenvironment even after rejection treatment. This is consistent with transcriptional signatures in circulating monocytes indicative of migration and differentiation into peripheral tissues. Persistent macrophage infiltration has been reported in human kidney transplantation, where their presence is associated not only with the resolution of inflammation but also with progression to fibrosis and poorer long-term graft survival, partly through pathways such as transforming growth factor β1 signaling[37,38]. This dual role highlights the importance of monitoring macrophage polarization in xenotransplantation, as sustained M2 infiltration may signal a risk for chronic graft injury and impaired outcomes. Clinically, these findings highlight that current immunosuppressive regimens targeting adaptive immunity are insufficient to control innate immune activation in xenotransplantation. Future xenograft recipients may benefit from therapies specifically targeting innate immunity, such as IL-1 or IL-6 blockade, to improve graft outcomes.

In addition to pharmacologic strategies, future engineering of porcine donors could focus on reducing innate immune activation by targeting key inflammatory pathways identified in this study. Given the prominent upregulation of IL-1 signaling (also observed by Kawai et al.[5]), graft-specific expression of human IL-1 receptor antagonist could offer localized suppression of cytokine-driven inflammation. Introducing immunoregulatory molecules such as PD-L1 may further help modulate residual T cell and macrophage activity through checkpoint inhibition. These strategies, combined with existing transgenes that address complement activation, coagulation and macrophage phagocytosis, could provide a comprehensive approach to reducing xenograft-induced innate immune activation. Collectively, such next-generation genetic modifications hold promise for enhancing graft compatibility, reducing reliance on systemic immunosuppression and improving long-term outcomes in clinical xenotransplantation.

This study is limited by its single patient design, necessitating validation in larger xenotransplantation trials to confirm the generalizability of our findings. The short follow-up period also limits our understanding of long-term immune adaptation and graft survival. In addition, the limited number of biopsies restricted the ability to fully monitor tissue-based immune responses. Given the importance of the tissue microenvironment in graft outcomes, future studies should incorporate more frequent and systematic biopsy sampling to comprehensively assess immune dynamics over time.

In summary, this study provides a detailed high-dimensional immune characterization of pig-to-human kidney transplantation into a living recipient. While demonstrating the feasibility of kidney xenotransplantation, our findings reveal that targeting adaptive immunity alone may be insufficient. Achieving durable graft survival and favorable patient outcomes will require refined strategies to modulate innate immune activation, prevent early T cell-mediated rejection, and implement more sensitive and dynamic monitoring approaches. Advancing xenotransplantation as a sustainable solution to organ shortage will require next-generation immunosuppressive regimens and real-time diagnostic tools.

Online content

Any methods, additional references, Nature Portfolio reporting summaries, source data, extended data, supplementary information, acknowledgements, peer review information; details of author contributions and competing interests; and statements of data and code availability are available at https://doi.org/10.1038/s41591-025-04053-3.

References

1. United States Renal Data System. *2024 USRDS Annual Data Report: Epidemiology of Kidney Disease in the United States* (National Institutes of Health, National Institute of Diabetes and Digestive and Kidney Diseases, 2024).
2. Teitelbaum, I. Peritoneal dialysis. *N. Engl. J. Med.* **385**, 1786–1795 (2021).
3. Aufhauser, D. D. Jr et al. Impact of prolonged dialysis prior to renal transplantation. *Clin. Transplant.* **32**, e13260 (2018).
4. Anand, R. P. et al. Design and testing of a humanized porcine donor for xenotransplantation. *Nature* **622**, 393–401 (2023).
5. Kawai, T. et al. Xenotransplantation of a porcine kidney for end-stage kidney disease. *N. Engl. J. Med.* **392**, 1933–1940 (2025).
6. Eisenson, D. et al. Consistent survival in consecutive cases of life-supporting porcine kidney xenotransplantation using 10GE source pigs. *Nat. Commun.* **15**, 3361 (2024).

7. Kim, S. C. et al. Long-term survival of pig-to-rhesus macaque renal xenografts is dependent on CD4 T cell depletion. *Am. J. Transpl.* **19**, 2174–2185 (2019).
8. Adams, A. B. et al. Iscalimab combined with transient tesidolumab prolongs survival in pig-to-rhesus monkey renal xenografts. *Xenotransplantation* **31**, e12880 (2024).
9. Tasaki, M. et al. Rituximab treatment prevents the early development of proteinuria following pig-to-baboon xeno-kidney transplantation. *J. Am. Soc. Nephrol.* **25**, 737–744 (2014).
10. Feng, J., Lu, S., Ding, Y., Zheng, M. & Wang, X. Homocysteine activates T cells by enhancing endoplasmic reticulum-mitochondria coupling and increasing mitochondrial respiration. *Protein Cell* **7**, 391–402 (2016).
11. Haghikia, A. et al. Dietary fatty acids directly impact central nervous system autoimmunity via the small intestine. *Immunity* **43**, 817–829 (2015).
12. Tan, H. et al. Ketoglutaric acid can reprogram the immunophenotype of triple-negative breast cancer after radiotherapy and improve the therapeutic effect of anti-PD-L1. *J. Transl. Med.* **21**, 462 (2023).
13. Kim, H. Y. et al. Indoxyl sulfate (IS)-mediated immune dysfunction provokes endothelial damage in patients with end-stage renal disease (ESRD). *Sci. Rep.* **7**, 3057 (2017).
14. Poesen, R. et al. Renal clearance and intestinal generation of p-cresyl sulfate and indoxyl sulfate in CKD. *Clin. J. Am. Soc. Nephrol.* **8**, 1508–1514 (2013).
15. Kim, H. Y. et al. Uremic toxin indoxyl sulfate induces trained immunity via the AhR-dependent arachidonic acid pathway in end-stage renal disease (ESRD). *eLife* **12**, RP87316 (2024).
16. Michalski, C. et al. DDIT4L regulates mitochondrial and innate immune activities in early life. *JCI Insight* **9**, e172312 (2024).
17. Cros, A. & Segura, E. IL1R2 acts as a negative regulator of monocyte recruitment during inflammation. *Eur. J. Immunol.* **55**, e202451468 (2025).
18. Ji, L. & Guo, W. Single-cell RNA sequencing highlights the roles of C1QB and NKG7 in the pancreatic islet immune microenvironment in type 1 diabetes mellitus. *Pharmacol. Res.* **187**, 106588 (2023).
19. Lee, Y. S. et al. CX(3)CR1 differentiates F4/80(low) monocytes into pro-inflammatory F4/80(high) macrophages in the liver. *Sci. Rep.* **8**, 15076 (2018).
20. Grasset, M. F., Gobert-Gosse, S., Mouchiroud, G. & Bourette, R. P. Macrophage differentiation of myeloid progenitor cells in response to M-CSF is regulated by the dual-specificity phosphatase DUSP5. *J. Leukoc. Biol.* **87**, 127–135 (2010).
21. Trizzino, M. et al. EGR1 is a gatekeeper of inflammatory enhancers in human macrophages. *Sci. Adv.* **7**, eaaz8836 (2021).
22. Cervenka, I., Agudelo, L. Z. & Ruas, J. L. Kynurenines: tryptophan's metabolites in exercise, inflammation, and mental health. *Science* **357**, eaaf9794 (2017).
23. Dennis, E. A. & Norris, P. C. Eicosanoid storm in infection and inflammation. *Nat. Rev. Immunol.* **15**, 511–523 (2015).
24. Zhang, S. et al. Nuclear adenine activates hnRNPA2B1 to enhance antibacterial innate immunity. *Cell Metab.* **37**, 413–428 (2025).
25. Rosales, I. A. et al. Banff human organ transplant transcripts correlate with renal allograft pathology and outcome: importance of capillaritis and subpathologic rejection. *J. Am. Soc. Nephrol.* **33**, 2306–2319 (2022).
26. Aubert, O. et al. Cell-free DNA for the detection of kidney allograft rejection. *Nat. Med.* **30**, 2320–2327 (2024).
27. Matz, M. et al. The regulation of interferon type I pathway-related genes RSAD2 and ETV7 specifically indicates antibody-mediated rejection after kidney transplantation. *Clin. Transpl.* **32**, e13429 (2018).
28. Van Loon, E. et al. Biological pathways and comparison with biopsy signals and cellular origin of peripheral blood transcriptomic profiles during kidney allograft pathology. *Kidney Int.* **102**, 183–195 (2022).
29. Alloway, R. R. et al. Rabbit anti-thymocyte globulin for the prevention of acute rejection in kidney transplantation. *Am. J. Transpl.* **19**, 2252–2261 (2019).
30. Loupy, A. et al. Immune response after pig-to-human kidney xenotransplantation: a multimodal phenotyping study. *Lancet* **402**, 1158–1169 (2023).
31. Schmauch, E. et al. Integrative multi-omics profiling in human decedents receiving pig heart xenografts. *Nat. Med.* **30**, 1448–1460 (2024).
32. Wang, Y. et al. Pig-to-human kidney xenotransplants using genetically modified minipigs. *Cell Rep. Med.* **5**, 101744 (2024).
33. Ma, D. et al. Kidney transplantation from triple-knockout pigs expressing multiple human proteins in cynomolgus macaques. *Am. J. Transpl.* **22**, 46–57 (2022).
34. Yamamoto, T. et al. Old World monkeys are less than ideal transplantation models for testing pig organs lacking three carbohydrate antigens (triple-knockout). *Sci. Rep.* **10**, 9771 (2020).
35. Pan, W. et al. Cellular dynamics in pig-to-human kidney xenotransplantation. *Med.* **5**, 1016–1029 (2024).
36. Ezzelarab, M. B. et al. Systemic inflammation in xenograft recipients precedes activation of coagulation. *Xenotransplantation* **22**, 32–47 (2015).
37. Guillen-Gomez, E. et al. Early macrophage infiltration and sustained inflammation in kidneys from deceased donors are associated with long-term renal function. *Am. J. Transpl.* **17**, 733–743 (2017).
38. Brasen, J. H. et al. Macrophage density in early surveillance biopsies predicts future renal transplant function. *Kidney Int.* **92**, 479–489 (2017).
39. Bai, H. et al. Identification of TCR repertoires in asymptomatic COVID-19 patients by single-cell T-cell receptor sequencing. *Blood Cells Mol. Dis.* **97**, 102678 (2022).
40. Yu, C. et al. Mucosal-associated invariant T cell responses differ by sex in COVID-19. *Med.* **2**, 755–772.e5 (2021).
41. Amrute, J. M. et al. Cell specific peripheral immune responses predict survival in critical COVID-19 patients. *Nat. Commun.* **13**, 882 (2022).

[1]Center for Transplantation Sciences, Department of Surgery, Massachusetts General Hospital and Harvard Medical School, Boston, MA, USA. [2]Institut Pasteur de São Paulo, São Paulo, Brazil. [3]Department of Clinical and Toxicological Analyses, University of São Paulo, São Paulo, Brazil. [4]Department of Pathology, Massachusetts General Hospital and Harvard Medical School, Boston, MA, USA. [5]Laboratory of Systems Pharmacology, Department of Systems Biology, Ludwig Center at Harvard, Harvard Medical School, Boston, MA, USA. [6]Department of Pathology, Brigham and Women's Hospital, Harvard Medical School, Boston, MA, USA. [7]Department of Cancer Biology, Dana-Farber Cancer Institute, Boston, MA, USA. [8]Karius Inc., Redwood City, CA, USA. [9]Hospital Israelita Albert Einstein, São Paulo, Brazil. [10]These authors jointly supervised this work: Thiago J. Borges, Leonardo V. Riella.
✉e-mail: tdejesusborges@mgh.harvard.edu; lriella@mgh.harvard.edu

Methods

Kidney xenotransplantation and sample collection

An EGEN-2784 gene-edited pig kidney was transplanted into a 62-year-old male patient with end-stage kidney disease, recently described in ref. 5. A Yucatan miniature pig was genetically engineered with 69 genomic modifications. These included the deletion of three major glycan antigens, the inactivation of porcine endogenous retroviruses and the insertion of seven human transgenes (*TNFAIP3*, *HMOX1*, *CD47*, *CD46*, *CD55*, *THBD* and *EPCR*). The immunosuppressive protocol included antithymocyte globulin (ATG, 1.5 mg kg^{-1} on days −2 and −1), rituximab (anti-CD20, 1,000 mg on day −3), Fc-modified anti-CD154 monoclonal antibody (tegoprubart, 20 mg kg^{-1} on days −3, −2, −1, 1, 3, 7 and weekly thereafter) and anti-C5 antibody (ravulizumab, 3,330 mg on days −1, 7 and 28). This regimen was combined with standard maintenance immunosuppression consisting of tacrolimus, mycophenolic acid (540 mg twice daily) and glucocorticoids starting on day 0. On post-transplant day 8, a biopsy revealed Banff grade 2A TCMR without signs of thrombotic microangiopathy or antibody-mediated rejection. Treatment included a 500-mg pulse of methylprednisolone and anti-IL-6 receptor monoclonal antibody (tocilizumab, 8 mg kg^{-1}). Additional 500-mg methylprednisolone pulses were given on days 9 and 10, along with ATG (1.5 mg kg^{-1}). Tacrolimus and mycophenolic acid doses were increased. Due to C3 deposition seen in the biopsy, pegcetacoplan, a targeted C3 and C3b inhibitor, was administered. However, as there was no evidence of antibody-mediated rejection, no further doses of tocilizumab were given.

Peripheral blood was collected for serum and plasma at pretransplantation (day −3), post-xenotransplantation (days 13, 20, 26, 33 and 51) and during suspected rejection (day 7 post-transplantation). Blood was collected in heparinized tubes for PBMCs isolation at pretransplantation (day −3) and post-xenotransplantation (days 13, 20, 26 and 33). Blood was also collected in Paxgene tubes for RNA profiling (days −3 and 7) and post-xenotransplantation (day 26). The sample collection schedule is shown in Fig. 1a. The patient provided written informed consent, as approved by the MGH Human Research Committee (IRB no: 2023P003631).

Recipient PBMC and serum isolation

PBMCs were isolated using density gradient centrifugation using Ficoll-Paque solution (GE HealthCare), counted and cryopreserved in heat-inactivated Human AB serum (GeminiBio) with 10% dimethylsulfoxide (Sigma-Aldrich) in liquid nitrogen. The serum was isolated and stored at −80 °C until further analyses.

Single-cell transcriptomics

Cryopreserved PBMCs were thawed and washed two times with PBS ×1. Cells were then counted using a Countess II Automated Cell Counter and loaded for scRNA-seq using ×10 Genomics Chromium Single Cell 30 Kit (v3.1 Chemistry). We preprocessed the reads with pyroe 0.9.0, Salmon 1.10.3 and alevin 0.10.0 packages with the reference genome GRCh38.p14 v46 from Gencode, and performed the downstream analysis with Seurat 5.1.0.

Longitudinal recipient samples were integrated with 22 external healthy control samples from 3 publicly available PBMC datasets (GEO accessions GSE165080, GSE171555 and GSE192391) using Harmony 1.2.0. The GSE165080 dataset consisted of 6 female samples and 5 male samples with a mean age of 43.1 ± 7.94 years[39]; the GSE171555 dataset included 3 female and 2 male samples[40]; and the GSE192391 dataset consisted of 4 female and 2 male samples[41]. Age information was not available for the GSE171555 and GSE192391 datasets.

Before integration, each dataset underwent independent quality control filtering followed by normalization using the Seurat SCTransform function. Based on an empirical evaluation of the distributions of the number of Unique Molecular Identifiers (UMIs) (nCount_RNA), number of detected genes (nFeature_RNA), log-transformed gene-to-UMI ratio (log10GenesPerUMI) and mitochondrial gene expression ratio (mitoRatio), the following filters were applied: GSE165080: nCount_RNA ≥ 1,800; nFeature_RNA ≥ 900 and <2,500; log10GenesPerUMI ≥ 0.84 and mitoRatio < 22%. GSE192391: nCount_RNA ≥ 1,800; nFeature_RNA ≥ 1,000 and <2,500; log10GenesPerUMI ≥ 0.84 and mitoRatio < 10%. GSE171555: nCount_RNA ≥ 1,800; nFeature_RNA ≥ 900 and <2,500; log10GenesPerUMI ≥ 0.84 and mitoRatio < 8%. Recipient samples: nCount_RNA ≥ 350; nFeature_RNA ≥ 300 and <2,500; log10GenesPerUMI ≥ 0.84 and mitoRatio < 10%. An additional gene filtering step was applied to each dataset, retaining only genes expressed (that is, nonzero counts) in at least 10 cells.

After integration, marker genes for each cluster were identified using the FindAllMarkers function following PrepSCTFindMarkers. Clusters were manually annotated into cell types based on the expression of the marker genes (Extended Data Fig. 3). A first round of annotation was performed at clustering resolutions of 0.2 and 0.4, resulting in 13 annotated cell types: $CD4^+$ T cells, $CD8^+$ T cells, erythrocytes, B cells, $CD16^+$ monocytes, megakaryocytes/platelets, naive-like $CD8^+$ T cells, plasmacytoid dendritic cells, conventional dendritic cells, two subsets of $CD14^+$ monocytes and two subsets of NK cells. A second round of annotation was performed after sub-clustering aggregated monocyte and T cell subsets, followed by marker gene identification. This round annotated a third subset of $CD14^+$ monocytes, naive-like $CD4^+$ T cells, $CD8^+$ MAIT cells and T_{reg} cells. Single cells expressing canonical marker genes of at least two major cell types were assumed to be doublets and excluded from the Seurat object.

Gene sets of interest across time were identified empirically by calculating the average log_2 fold change at each time point relative to the pretransplant baseline. This analysis was performed separately for $CD14^+$ monocyte subsets, $CD16^+$ monocytes and NK cell subsets. Genes were then ranked based on the absolute average log_2 fold change to prioritize those with the most pronounced temporal shifts in expression.

Peripheral blood bulk transcriptomics

Venous blood collected at different time points and stored in PAXgene tubes at −80 °C were used for bulk RNA-seq. To process the bulk RNA-seq, we used FastQC 0.12.0 with standard parameters to evaluate the quality of the reads. We trimmed the adapters with Fastp 1.0.1 and quantified the abundance of transcripts with Salmon 1.10.3. We used the human reference transcriptome and the annotation named GRCh38.p14 v.46 from Gencode as the transcriptome reference. We used tximport 1.32.0 to import the abundance files and DESeq2 was used to harmonize samples. The same process was used for the public dataset (GSE120649 (ref. 27)). We used SRA tool 2.10.7 to download the public fastq files.

Proteomics

To perform proteomics analysis from serum samples, 11,000 markers were measured using SomaScan analysis (SomaLogic). This analysis was performed at the BIDMC Genomics, Proteomics, Bioinformatics and Systems Biology Center using the SomaScan Assay Kit for human serum, covering ~11,000 proteins. The expression counts were standardized using the median of hybridization controls. The outliers were flagged based on the limit of variation of 0.4–2.5 of the ratios.

Metabolomics

Untargeted metabolite analysis was performed using a Q Exactive HF-X mass spectrometer equipped with a HESI II probe and coupled to a Vanquish binary ultra-performance liquid chromatography system (Thermo Fisher Scientific). Each sample underwent two chromatographic separations. For both methods, 5 µl of the sample was injected into a BEH Z-HILIC column (100 × 2.1 mm, 1.7 µm, Waters). The first separation was conducted at pH 9, using 15 mM ammonium bicarbonate (Merck) in 90% water and 10% acetonitrile as mobile phase A, then 95% acetonitrile and 5% water as mobile phase B. The gradient was applied at a flow rate of 0.225 ml per min, following a method adapted from[42], and the mass spectrometer operated in negative mode. The second separation followed the method of Mülleder et al.[43], with mobile phases A and B buffered with 10 mM ammonium formate and 45 mM formic acid (pH 2.7). Mobile phase A consisted of a 1:1 acetonitrile to water mixture, while mobile phase B contained 95:5:5 acetonitrile to water to methanol. Chromatography was conducted at 40 °C (column oven) and 4 °C (autosampler), with a gradient flow rate of 0.4 ml per min as follows: an initial hold at 95% B for 0.75 min, a linear decrease to 30% B from 0.75 to 3.00 min, followed by a 1.00 min isocratic hold at 30% B. Mobile phase B was then returned to 95% over 0.50 min, with re-equilibration under initial conditions. Mass spectrometry was performed in positive mode. Data acquisition was carried out in full-scan mode, with the spray voltage set to 3 kV (negative mode) or 3.5 kV (positive mode). The capillary temperature was maintained at 320 °C, the HESI probe at 300 °C, the sheath gas at 40 U, the auxiliary gas at 8 U and the sweep gas at 1 U. The resolving power was set to 120,000. An untargeted metabolite library was generated using top-15 DDA acquisitions on a pooled study sample, with MS1 and MS2 resolutions of 60,000 and 30,000, respectively.

Raw data files (.raw) were processed using MZmine 4.5[44] and emzed[45]. Metabolite MS2 spectra were compared against HMDB, GNPS, MassBank and MoNA databases using spectral library matching (ref to DDA_library). In addition, retention times and *m*/*z* values from full-scan acquisitions of a pooled study sample were cross-referenced with an in-house database containing retention times of authenticated standards (Human Endogenous Metabolite Compound Library Plus L2501, TargetMol). Internal standards were integrated via emzed, and raw peak areas were normalized by dividing by sample biomass and the mean internal standard area.

Isolation of lymph node cells

On the day of the transplant, an iliac lymph node was harvested during the surgery for cell isolation. A lymph node from a patient who did not receive ATG was used as a control. The tissues were minced and digested with 500 U ml^{-1} collagenase D (Roche) for 30 min at 37 °C, followed by incubation with 0.1 M EDTA in PBS, pH 7.2, buffer for 5 min before a final suspension in 5 mM EDTA (Gibco), 1% FBS (Gibco) in × 1 PBS, pH 7.2 (Boston BioProducts). Isolated cells were then mechanically dissociated through a 70-µm cell strainer (Corning) in a 50-ml tube, and red blood cells were lysed using hypotonic ACK buffer (Gibco). Cells were then counted and cryopreserved in heat-inactivated human AB serum (GeminiBio) with 10% dimethylsulfoxide (Sigma-Aldrich) in liquid nitrogen.

Flow cytometry

Monitoring of immune cells over time was performed using 100 µl of whole blood. Cells were stained with surface antibodies for 30 min at room temperature, followed by incubation with 1× BD FACS Lysing Solution (BD Biosciences) for 10 min at room temperature for lysing red blood cells. We also stained cells isolated from human lymph nodes. Cells were thawed, washed twice and Fc-blocked (TruStain FcX, combination of anti-human CD16 (clone 3G8), CD32 (clone FUN-2) and CD64 (clone 10.1) antibodies, BioLegend, cat. no.: 422302) for 20 min before staining for surface markers for 30 min in FACS buffer (2% FBS in PBS × 1) on ice. The information about the antibodies used is shown in Supplementary Table 1. Stained cells were analyzed on an LSR Fortessa X-20 flow cytometer (BD Biosciences) with FACSDiva software (BD Biosciences) for all experiments. Data were analyzed using FlowJo software (Tree Star) in all experiments. Viable cells were selected based on the staining with LIVE/DEAD Fixable Blue Dead Cell Stain Kit (1:1000, Thermo Fisher, cat. no.: L23105) before Fc-blocking. Gating strategies for PBMC analysis were as previously described and can be found in Supplementary Fig. 2.

Innate immunity functional assay

Recipient's PBMCs from different time points were thawed and washed twice with RPMI 1640 (Gibco) containing 10% FBS (GeminiBio) and ×1 pen/strep (Gibco) (complete RPMI), and then resuspended in complete RPMI. In a 96-well round-bottomed tissue culture plate at a volume of 100 µl, 4 × 105 cells per well were seeded. Cells were stimulated with 100 µl of either complete RPMI (controls) or a mixture of bacterial and viral TLR ligands (0.025 µg ml^{-1} LPS, 10 µg ml^{-1} Pam3CSK4, 4 µg ml^{-1} R848, 25 µg ml^{-1} poly I:C—all from Invivogen). PBMCs from each sample were stimulated in duplicates. After 24 h of incubation at 37 °C and 5% CO_2, supernatants were obtained for Luminex analysis using the premixed ProcartaPlex Human Immune Monitoring Panel 65-plex (Thermo Fisher), including APRIL, BAFF, CXCL13, CD30, CD40L, CXCL5, CCL11, CCL24, CCL26, fibroblast growth factor-2 (FGF-2), CX3CL1, G-CSF, GM-CSF, CXCL1, hepatocyte growth factor, IFNα, IFNγ, IL-1α, IL-1β, IL-10, IL-12p70, IL-13, IL-15, IL-16, IL-17A, IL-18, IL-2, IL-20, IL-21, IL-22, IL-23, IL-27, IL-2R, IL-3, IL-31, IL-4, IL-5, IL-6, IL-7, IL-8, IL-9, CXCL10, CXCL11, LIF, CCL2, CCL7, CCL8, lymphotoxin-alpha, macrophage colony-stimulating factor, MDC, MIF, CXCL9, CCL3, CCL4, CCL20, MMP-1, nerve growth factor beta (NGF-β), SCF, SDF-1α, TNF, TNF-RII, TRAIL, TSLP, TWEAK and vascular endothelial growth factor A (VEGF-A). We read the assay in a Luminex200 machine, and data with a bead count <20 were excluded. Samples from the time points from one individual were measured on the same plate to mitigate the effect of potential plate-based technical variation on calculated fold changes between time points.

Intragraft tissue bulk transcriptomics

Bulk mRNA analysis was performed from formalin-fixed paraffin-embedded xenograft biopsies and a sample from the nontransplanted contralateral donor kidney, using the nCounter instrument (Nanostring) combined with the Banff Human Organ Transplant panel, following the methods and data analysis previously documented for human allograft biopsies[25]. The probe sequences were screened for homology with pig and NHP transcripts by a specialist at the manufacturer company (NanoString). We used probes from the panel that had >85% homology with porcine sequences for parenchymal cells or endothelium (*n* = 235 probes) and all probes for human leukocytes, similar to those used previously in pig-to-human xenografts[5,30]. Normalization was performed using seven housekeeping probes with >90% homology with the corresponding porcine transcripts. Pathways were manually curated from prior publications[25,46–48] and KEGG Pathways (https://www.kegg.jp/kegg/pathway.html), Gene Ontology (geneontology.org) and Reactome (reactome.org) repositories. Cell types from tissue bulk were assessed with marker genes[49].

Xenograft histopathologic analysis

Biopsy tissue was processed using standard kidney biopsy methods for light microscopy. hematoxylin and eosin samples were scored using the current Banff criteria[50,51].

Multiplex immunofluorescence

Frozen slides from the donor collateral kidney biopsy and xenografts at days 8 and 34 were processed for multiplex imaging on the Orion platform (RareCyte), following Lin et al.[52]. An Orion multiplex antibody panel was used to profile immune cell subsets (Supplementary Table 2). In brief, slides were thawed at room temperature and then fixed in 4% paraformaldehyde in PBS for 45 min. They were washed in Tris-buffered saline, permeabilized in 0.5% Triton X-100 in Tris-buffered saline for 5 min at room temperature, washed once in Tris-buffered saline and once in PBS, and treated with 4.5% H_2O_2/24 mM NaOH in PBS (hydrogen peroxide solution) to reduce autofluorescence. After a surfactant wash and enhancer treatment, slides were incubated overnight at 4 °C with ArgoFluor-conjugated antibodies and Hoechst 33342. The next day, slides were washed extensively in PBS, mounted in ArgoFluor mounting medium (RareCyte 42-1214-000), and imaged on an Orion microscope.

Fluorophores were then quenched with hydrogen peroxide solution, and a second round of overnight 4 °C staining was performed with a different set of ArgoFluor-conjugated antibodies (Supplementary Table 2) plus Hoechst 33342, followed by mounting and imaging.

Image stitching, segmentation and single-cell quantification were carried out using the MCMICRO pipeline[53]. A Gaussian mixture model implemented in MATLAB (MathWorks)[54] excluded cells exhibiting excessive autofluorescence. Gating strategies were defined as follows: CD4 T cells: HLA-ABC$^+$, CD45$^+$ and CD4$^+$; CD8 T cells: HLA-ABC$^+$, CD45$^+$ and CD8$^+$; M1 macrophages: HLA-ABC$^+$, CD68$^+$ and CD163$^-$; M2 macrophages: HLA-ABC$^+$ and CD163$^+$; NK cells: HLA-ABC$^+$, CD45$^+$ and NKG2A$^+$. The HLA-ABC marker recognizes human MHC I, thereby excluding from counts the few residual donor pig kidney-resident M2 macrophages with which the CD163 antibody cross-reacts (Extended Data Fig. 7).

DSA quantification using IgG binding assay

After pig donor blood collection, PBMCs were isolated using Lympholyte-Mammal Cell Separation Media (Cedarlane) according to the manufacturer's protocol. Using a V-bottom 96-well-plate, serum was serially diluted in PBS ×1 as follows: 1:4, 1:8, 1:16, 1:32, 1:64 and 1:128. Serum from a healthy human control and a Baboon previously transplanted with a pig kidney were used as negative and positive controls, respectively, along with different time points of the recipient serum. To avoid nonspecific binding sites, pig PBMCs (5 × 105 cells per well) were blocked with 10% heat-inactivated goat serum (R&D Systems, cat. no.: S13110H) for 20 mins at 4 °C. After two washes, pig PBMCs were incubated with serially diluted serum for 1 h at 4 °C and washed three times in cold PBS × 1. Next, pig PBMCs were incubated for 1 h at 4 °C with anti-human IgG Fc-APC (clone M1310G05, BioLegend). After two washes, cells were resuspended in a staining buffer (PBS, 1% of bovine serum albumin, 0.09% sodium azide). Stained cells were analyzed on an LSR Fortessa X-20 flow cytometer (BD Biosciences) with FACSDiva software (BD Biosciences) for all experiments. Data were analyzed using FlowJo software (Tree Star) in all experiments.

Cell-free DNA quantification

Karius retrieved porcine and human cfDNA using a protocol similar to that described by Blauwkamp et al.[55]. Briefly, plasma samples were initially processed by centrifugation to remove residual cells, after which cfDNA was extracted using a modified Mag-Bind cfDNA kit in automated liquid handling platforms. Sequencing libraries were prepared with dual-indexed Ovation Ultralow System kits and sequenced on Illumina NextSeq sequencers. The resulting reads underwent stringent bioinformatics processing, including alignment against human, porcine and microbial reference databases to distinguish human and porcine cfDNA fragments accurately. The concentration of each species' cfDNA was quantitatively estimated by normalizing against synthetic internal control molecules (WINC molecules), ensuring precise measurement of cfDNA abundance in plasma samples

Functional data analysis

We normalized all the data series to *z*-score with scikit-learn 1.6.1[56]. To analyze the data in time, we used scikit-fda 0.9.1[57]. With this package, we excluded outliers using the MS-Plot Outlier Detector method. We then used Fuzzy C-Means with l2-distance to cluster. We defined the optimal number of three clusters, calculating the silhouette score with scikit-learn 1.6.1. To plot the time series, we calculated the median with NumPy 2.2.0 and plotted the line and the violins with Matplotlib 3.8.0.

Network analysis

For the three clusters defined by functional data analysis, we used the *z*-score normalized proteomics data to calculate the nearest neighbors with scikit-fda 0.9.1, calculated the Louvain communities with NetworkX 3.4.2[58] based on the connectivity of the nearest neighbor's graph, followed by an enrichment analysis for each community with GSEApy 1.1.7[59]. After annotating the clusters based on GSEApy results, we trained a k-neighbors classifier with scikit-fda 0.9.1 on proteomics Louvain labels. We predicted the Louvain communities for *z*-score normalized metabolomics data. To plot networks, we used Netgraph 4.13.1 to annotate the nodes. We used the package adjustText 1.3.0 (https://github.com/Phlya/adjustText).

Cell population abundance—Cibersortx

After preprocessing the whole-blood bulk transcriptomic data, we normalized the expression counts with DESeq2. Next, we used the R package IOBR 0.99.8[60] to estimate the population abundance on whole blood using the LM22 and LM6 matrices without tumor optimization.

Intersection of differentially expressed proteins and genes

We calculated the $\log_2$ fold change between days 7 and 26 ($\log_2$[D7/D26]) for both transcriptomics and proteomics. Since we have only one sample, we selected the most relevant fold change by the first quartile of negative fold changes and the third quartile of positive fold changes to define downregulated and upregulated molecules, respectively. We found the intersection using Python native functions and performed an enrichment analysis with GSEApy 1.1.7[59]. To plot the Venn diagram, we used the venn 0.1.3 package.

Chord diagram visualization

A chord diagram was constructed using the circlize package 0.4.16[61] in R 4.4.2 to illustrate relationships between differentially expressed genes and proteins. Sectors representing upregulated and downregulated genes and proteins were color coded, and interconnections were drawn based on shared elements between sets. Edge transparency and arrow annotations were applied to improve interpretability.

Comparative analysis of xenograft and allograft rejection profiles

To maintain consistency, we reprocessed the public dataset GSE120649 (ref. 27) from whole-blood human kidney transplant recipients using the same pipeline used for the xenotransplant samples. We used a previously described transcriptional profile of human allograft rejection[28] to compare allo and xenotransplantation gene expression. To detect nonlinear correlation, we clustered the samples using the complete linkage method on the distance correlation metric with SciPy 1.11.4[62]. We used seaborn 0.13.2[63] to plot the cluster heatmap.

Reporting summary

Further information on research design is available in the Nature Portfolio Reporting Summary linked to this article.

Data availability

Quantification matrices for the resulting datasets (including PBMC scRNA-seq, bulk RNA-seq, proteomics and metabolomics) are available on Harvard Dataverse (https://doi.org/10.7910/DVN/KGQITG)[64].

Code availability

Custom codes and scripts are deposited on Harvard Dataverse (https://doi.org/10.7910/DVN/HMKPXS)[65].

References

42. Koley, S., Chu, K. L., Gill, S. S. & Allen, D. K. An efficient LC-MS method for isomer separation and detection of sugars, phosphorylated sugars, and organic acids. *J. Exp. Bot.* **73**, 2938–2952 (2022).
43. Mulleder, M., Bluemlein, K. & Ralser, M. A high-throughput method for the quantitative determination of free amino acids in saccharomyces cerevisiae by hydrophilic interaction chromatography-tandem mass spectrometry. *Cold Spring Harb. Protoc.* **9**, pdb.prot089094 (2017).

44. Schmid, R. et al. Integrative analysis of multimodal mass spectrometry data in MZmine 3. *Nat. Biotechnol.* **41**, 447–449 (2023).
45. Kiefer, P., Schmitt, U. & Vorholt, J. A. eMZed: an open source framework in Python for rapid and interactive development of LC/MS data analysis workflows. *Bioinformatics* **29**, 963–964 (2013).
46. Smith, R. N. et al. Utility of Banff Human Organ Transplant gene panel in human kidney transplant biopsies. *Transplantation* **107**, 1188–1199 (2023).
47. Reeve, J. et al. Molecular diagnosis of T cell-mediated rejection in human kidney transplant biopsies. *Am. J. Transplant.* **13**, 645–655 (2013).
48. Venner, J. M. et al. Molecular landscape of T cell-mediated rejection in human kidney transplants: prominence of CTLA4 and PD ligands. *Am. J. Transplant.* **14**, 2565–2576 (2014).
49. Danaher, P. et al. Advances in mixed cell deconvolution enable quantification of cell types in spatial transcriptomic data. *Nat. Commun.* **13**, 385 (2022).
50. Loupy, A. et al. The Banff 2015 Kidney Meeting report: current challenges in rejection classification and prospects for adopting molecular pathology. *Am. J. Transpl.* **17**, 28–41 (2017).
51. Naesens, M. et al. The Banff 2022 Kidney Meeting report: reappraisal of microvascular inflammation and the role of biopsy-based transcript diagnostics. *Am. J. Transpl.* **24**, 338–349 (2024).
52. Lin, J. R. et al. High-plex immunofluorescence imaging and traditional histology of the same tissue section for discovering image-based biomarkers. *Nat. Cancer* **4**, 1036–1052 (2023).
53. Schapiro, D. et al. MCMICRO: a scalable, modular image-processing pipeline for multiplexed tissue imaging. *Nat. Methods* **19**, 311–315 (2022).
54. Lin, J. R. et al. Multiplexed 3D atlas of state transitions and immune interaction in colorectal cancer. *Cell* **186**, 363–381 (2023).
55. Blauwkamp, T. A. et al. Analytical and clinical validation of a microbial cell-free DNA sequencing test for infectious disease. *Nat. Microbiol.* **4**, 663–674 (2019).
56. Pedregosa, F. et al. Scikit-learn: machine learning in Python. *J. Mach. Learn. Res.* **12**, 2825–2830 (2011).
57. Ramos-Carreño, C., Torrecilla, J. L., Carbajo-Berrocal, M., Marcos, P. & Suárez, A. scikit-fda: a Python package for functional data analysis. *J. Stat. Softw.* **109**, 1–37 (2024).
58. Hagberg, A., Swart, P. & Chult, D. Exploring network structure, dynamics, and function using NetworkX. In *Proc. 7th Python in Science Conference* (SciPy, 2008).
59. Fang, Z., Liu, X. & Peltz, G. GSEApy: a comprehensive package for performing gene set enrichment analysis in Python. *Bioinformatics* **39**, btac757 (2023).
60. Zeng, D. et al. IOBR: multi-omics immuno-oncology biological research to decode tumor microenvironment and signatures. *Front. Immunol.* **12**, 687975 (2021).
61. Gu, Z., Gu, L., Eils, R., Schlesner, M. & Brors, B. circlize implements and enhances circular visualization in R. *Bioinformatics* **30**, 2811–2812 (2014).
62. Virtanen, P. et al. SciPy 1.0: fundamental algorithms for scientific computing in Python. *Nat. Methods* **17**, 261–272 (2020).
63. Waskom, M. L. seaborn: statistical data visualization. *J. Open Source Softw.* **6**, 3021 (2021).
64. Taborda Ribas, G. Replication data for: high-resolution profiling of immune responses following gene-edited pig kidney xenotransplantation into a living human. *Harvard Dataverse* https://doi.org/10.7910/DVN/KGQITG (2025).
65. Taborda Ribas, G. Code for: high-resolution profiling of immune responses following gene-edited pig kidney xenotransplantation into a living human. *Harvard Dataverse* https://doi.org/10.7910/DVN/HMKPXS (2025).

Acknowledgements

We gratefully acknowledge the contributions of the eGenesis team, whose expertise in the development and care of genetically engineered porcine donors was essential to the success of this study. We are especially thankful to the patient and his family, whose courage and altruism made this groundbreaking clinical investigation possible. Their willingness to participate has advanced the field of transplantation and opened the door to new therapeutic possibilities for patients with end-stage organ failure. This work was supported by Massachusetts General Hospital. This work was partially supported by the National Institute of Health grant R01AI143887 to L.V.R., Fundação de Amparo à Pesquisa do Estado de São Paulo-FAPESP (grant no. 2018/14933-2) to H.I.N., the Brazilian National Council for Scientific and Technological Development (grant no. 1) to H.I.N. and a Calmette & Yersin PhD grant from the Pasteur Network to A.F.C.

Author contributions

Conceptualization: L.V.R., T.J.B., R.B.C., H.I.N. and T.K. Methodology: G.T.R., A.F.C., A.G., R.B.G, J.-Y.C., J.-R.L., B.A.R., M.S.L., S.B., I.A.R., H.I.N., R.B.C. and T.J.B. Software: G.T.R., A.F.C., J.P.A., A.G., J.-Y.C., J.-R.L., S.S., I.A.R., H.I.N., R.B.C. and T.J.B. Validation: G.T.R., A.F.C., J.P.A., A.G., J.-R.L., B.A.R., H.I.N. and T.J.B. Formal analysis: G.T.R., A.F.C., J.P.A., A.G., K.L., R.B.G, J.-Y.C., J.-R.L., C.T.A., B.A.R., M.S.L., S.B., I.A.R., H.I.N. and T.J.B. Investigation: G.T.R., A.F.C., J.P.A., A.G., L.M., K.L., R.B.G., J.-Y.C., J.-R.L., S.S., C.T.A., B.A.R., M.S.L., S.B., I.A.R., H.I.N. and T.J.B. Resources: L.V.R., T.J.B., R.B.C., H.I.N., T.K., I.A.R., S.S., G.T.R., A.F.C., J.P.A. and A.G. Data curation: G.T.R., A.F.C., A.G., T.J.B., L.M. I.A.R. and C.T.A. Visualization: G.T.R., A.F.C., J.P.A., A.G., J.-Y.C., I.A.R. and T.J.B. Supervision: L.V.R., T.J.B., R.B.C., H.I.N., T.K., S.B. and S.S. Project administration: L.V.R., T.J.B., R.B.C. and T.K. Writing—original draft: L.V.R., T.J.B., R.B.C., H.I.N. and T.K. Writing—review and editing: all authors.

Competing interests

The authors declare no competing interests.

Additional information

Extended data is available for this paper at https://doi.org/10.1038/s41591-025-04053-3.

Supplementary information The online version contains supplementary material available at https://doi.org/10.1038/s41591-025-04053-3.

Correspondence and requests for materials should be addressed to Thiago J. Borges or Leonardo V. Riella.

Peer review information *Nature Medicine* thanks Leo Buhler, Joshua Weiner and the other, anonymous, reviewer(s) for their contribution to the peer review of this work. Primary Handling Editor: Michael Basson, in collaboration with the *Nature Medicine* team.

Reprints and permissions information is available at www.nature.com/reprints.

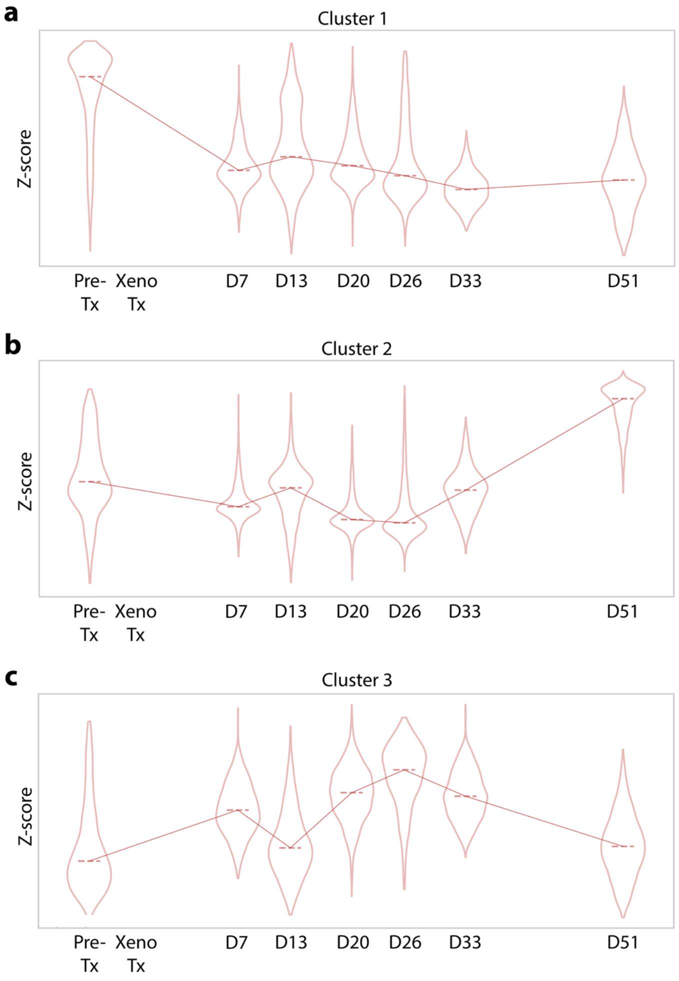

Extended Data Fig. 1 | Summarizing violin plots of clinical, metabolomics, and proteomics z-scores for each sample collection day. Three distinct analyte clusters were identified based on their temporal dynamics: one characterized by a progressive decline over time, which included 3433 features (**a**), another by a posttransplantation increase with 2599 features (**b**), and a third that exhibited no consistent temporal pattern, including 2792 features (**c**). The lines connect the median of features for each day for the three functional data analysis (FDA) clusters to highlight the different directions of each cluster. The clusters were defined by the semi-supervised clustering, which is based on FuzzyCMeans with pairwise L2 distance. The silhouette score optimized the number of clusters. More details about algorithms are in the methods section of the paper.

https://doi.org/10.1038/s41591-025-04053-3

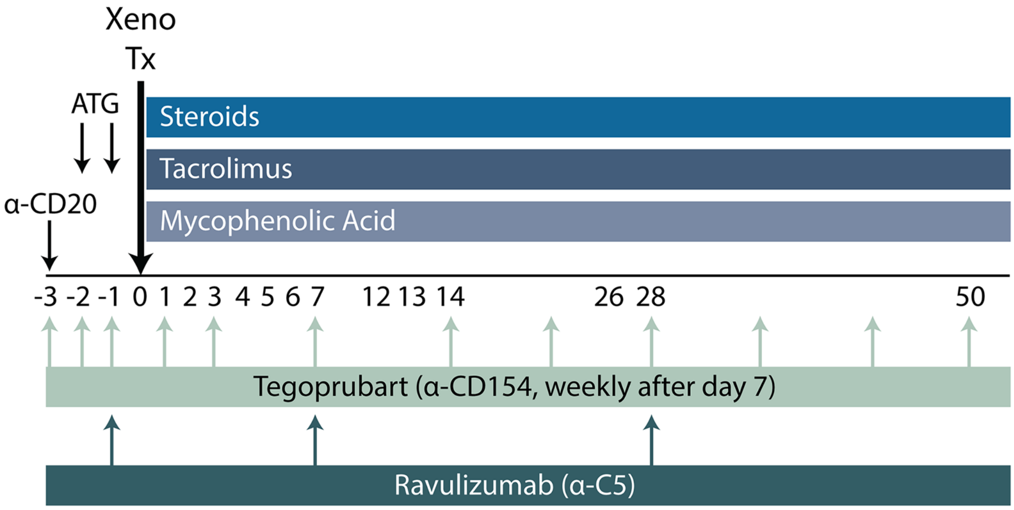

Extended Data Fig. 2 | Planned immunosuppressive regimen. ATG, antithymocyte globulin (1.5 mg/kg); α-CD20 (rituximab, 100 mg); Tegoprubart (Fc-modified α-CD154, 20 mg/kg); Ravulizumab (3330 mg); Mycophenolic acid (540 mg twice a day).

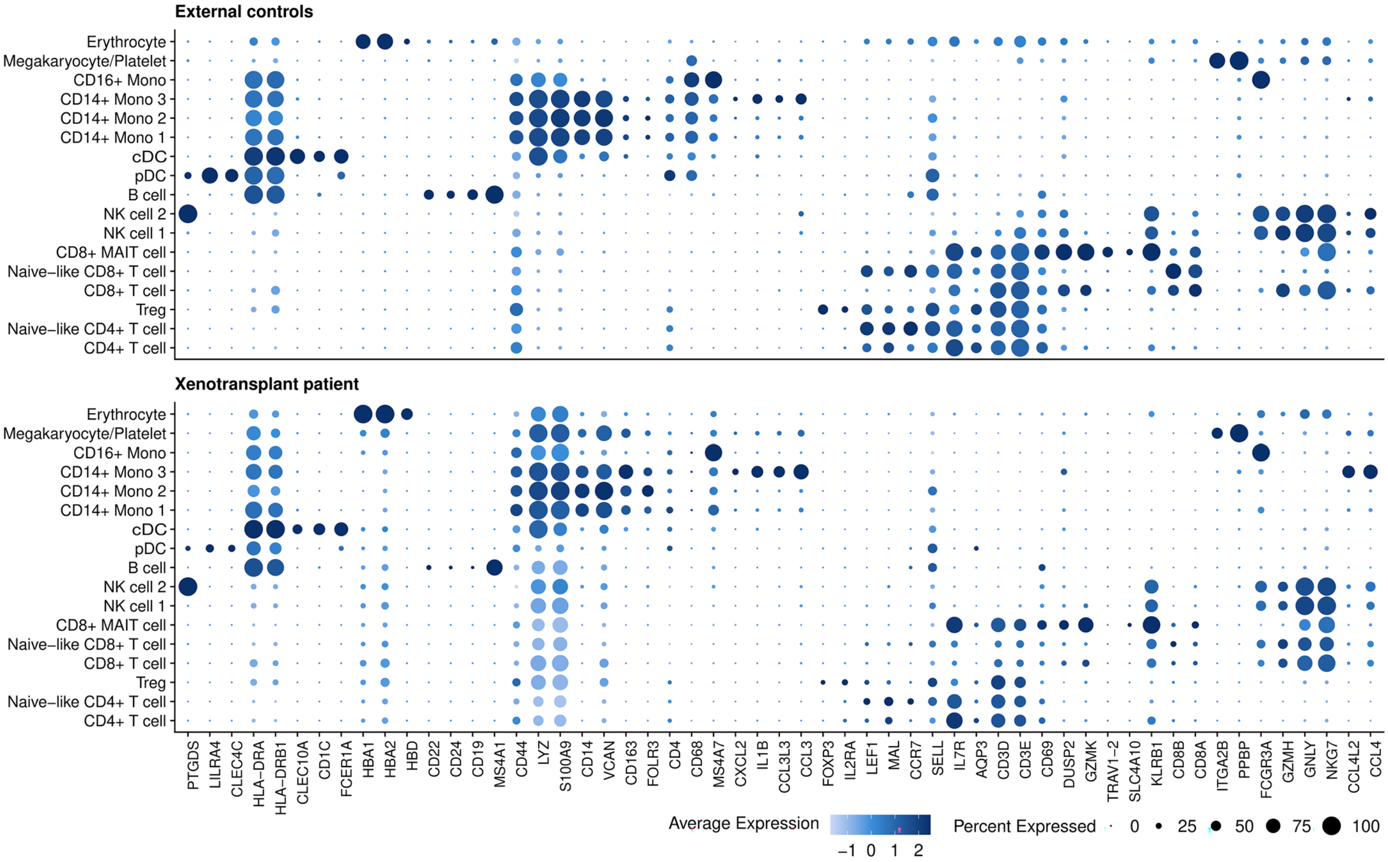

Extended Data Fig. 3 | Expression profiles of key marker genes used to identify major cell types. Bubble plots showing the expression levels and percentage of cells expressing marker genes used for cell type annotation of the 17 clusters observed in the scRNA-seq data. Related to Fig. 2a–c.

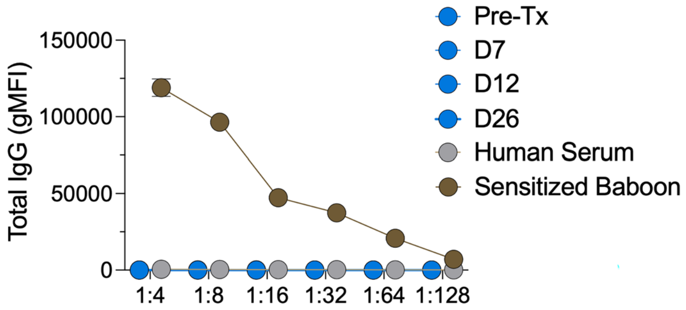

Extended Data Fig. 4 | Absence of donor-specific anti-porcine IgG antibodies. Donor porcine peripheral blood mononuclear cells (PBMCs) were incubated with serial dilutions (1:4, 1:8, 1:16, 1:32, 1:64, 1:128) of recipient serum collected at pre-transplant and days 7, 12, 21, and 26 posttransplant. Controls samples included serum from a healthy human individual and serum from a baboon previously transplanted with a porcine kidney (sensitized). Fluorescently labeled anti-human IgG antibody was used to quantify donor-specific antibody (DSA) levels by flow cytometry. The graph represents total IgG binding to porcine donor PBMCs, measured by geometric mean fluorescence intensity (gMFI). Data expressed as mean ± SD. Experiments were performed in triplicate.

https://doi.org/10.1038/s41591-025-04053-3

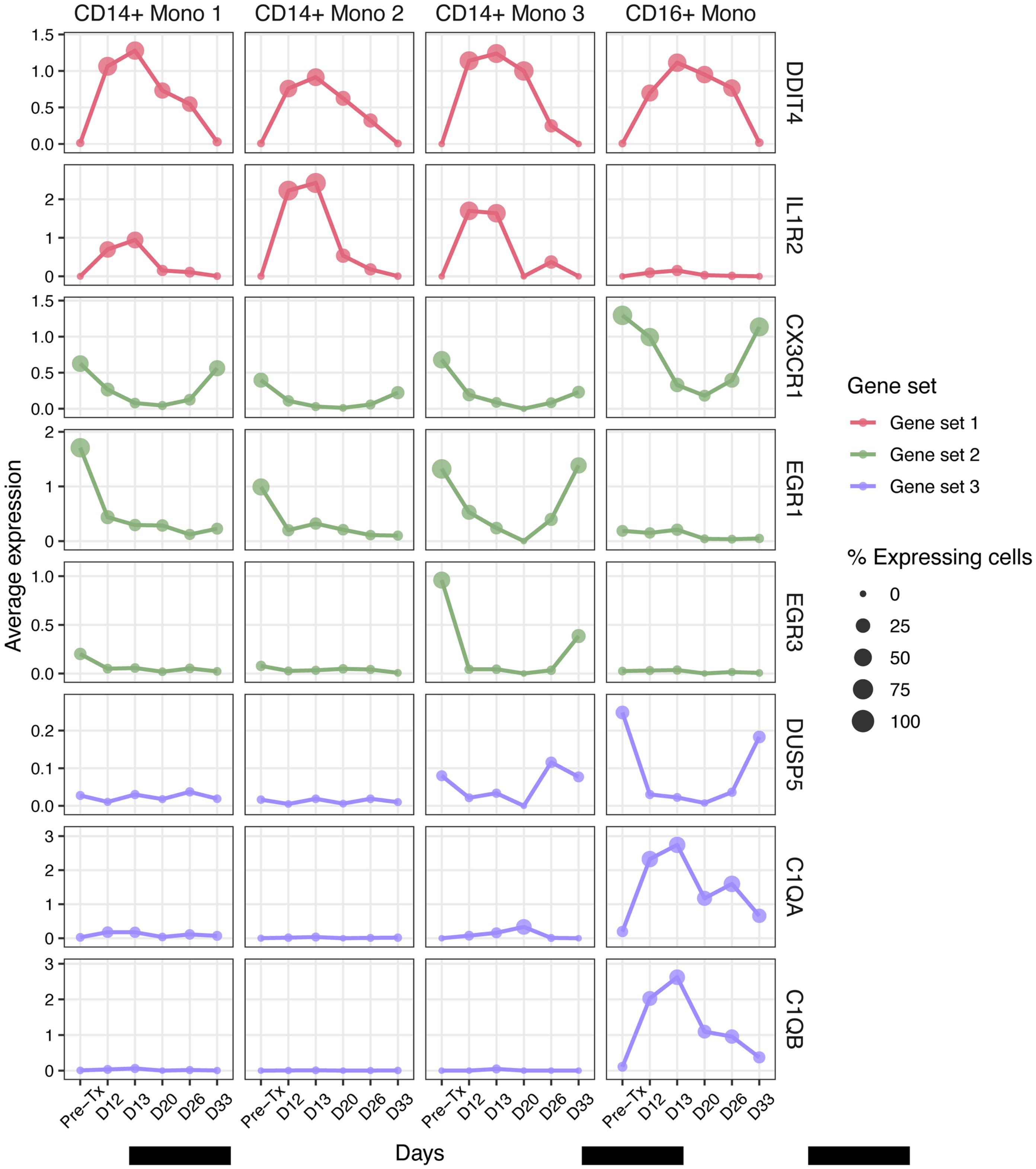

[redacted]

[redacted]

[redacted]

Extended Data Fig. 5 | Temporal gene expression dynamics of monocyte subsets following xenotransplantation. Gene expression profiles were analyzed in CD14$^+$ and CD16$^+$ monocyte subsets using the pre-transplant time point as baseline. Genes were ranked by the absolute average $\log_2$ fold-change across all time points to prioritize those with the most pronounced temporal shifts. Three major gene expression patterns were identified: gene set 1 (red) comprised genes upregulated after transplantation; gene set 2 (green) included genes that were downregulated; and gene set 3 (purple) contained genes predominantly expressed by CD16$^+$ monocytes. Related to Fig. 2a–c.

https://doi.org/10.1038/s41591-025-04053-3

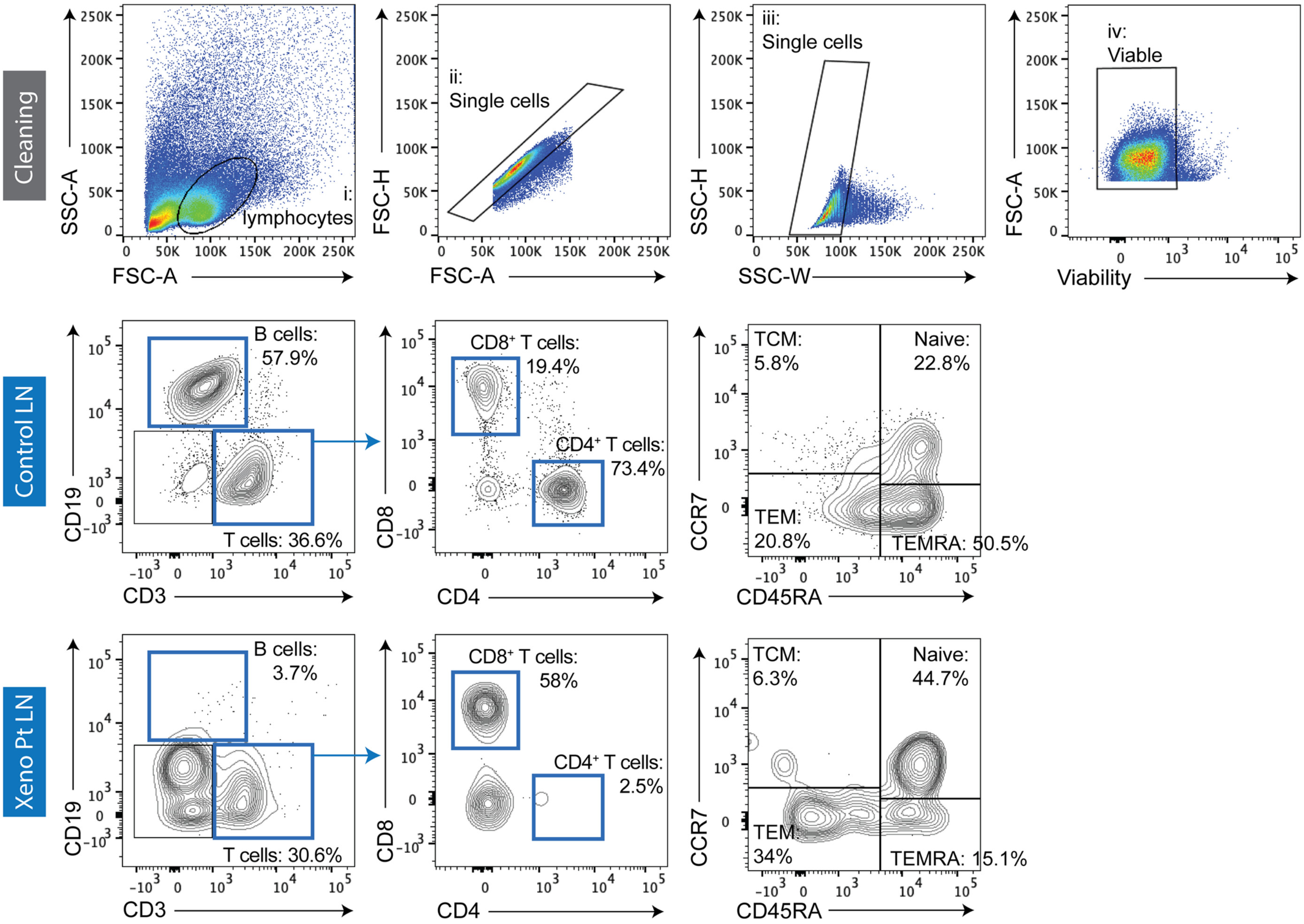

Extended Data Fig. 6 | Residual CD8⁺T cells in lymph nodes after induction therapy. Flow cytometry of an iliac lymph node (LN) from the kidney xenograft recipient removed during the transplant surgery (post-ATG infusion) and a comparison LN from a patient that did not receive ATG infusion.

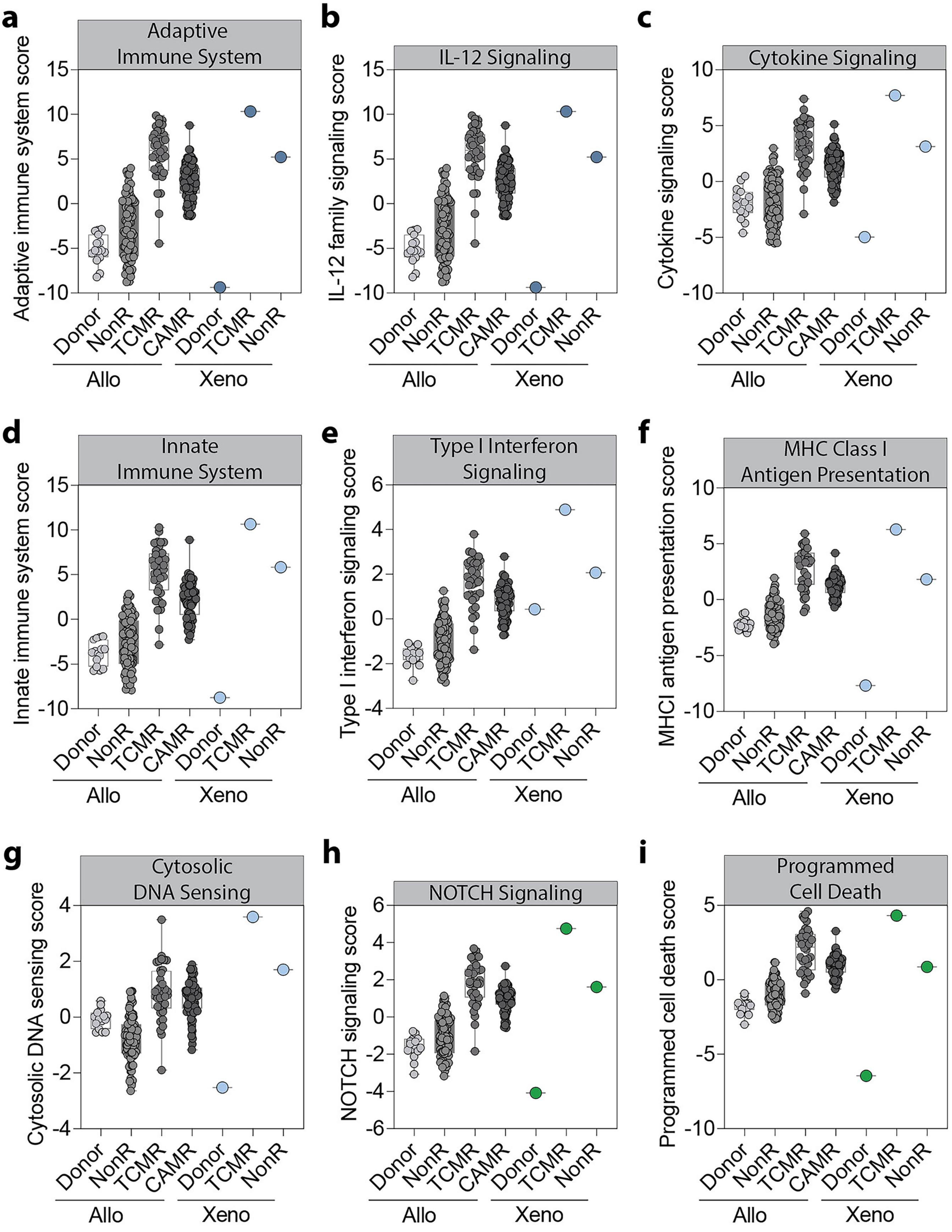

Extended Data Fig. 7 | See next page for caption.

Extended Data Fig. 7 | Biopsy cell-type- and immune signaling-specific transcriptional signatures. (**a**) adaptive immune system, (**b**) IL-12 family signaling, (**c**) cytokine signaling, (**d**) innate immune system, (**e**) type I interferon signaling, (**f**) MHC class I antigen presentation, (**g**) cytosolic DNA sensing, (**h**) NOTCH signaling, and (**i**) programmed cell death. Allogeneic (allo) donor (n = 15 samples), allo non-rejection (nonR, n = 84), allo T cell-mediated rejection (TCMR, n = 36), and allo chronic active antibody-mediated rejection (CAMR, n = 89). Data are represented as box plots with the center line representing the median, and the box limits are the minimum and maximum quartiles. All data points are displayed.

https://doi.org/10.1038/s41591-025-04053-3

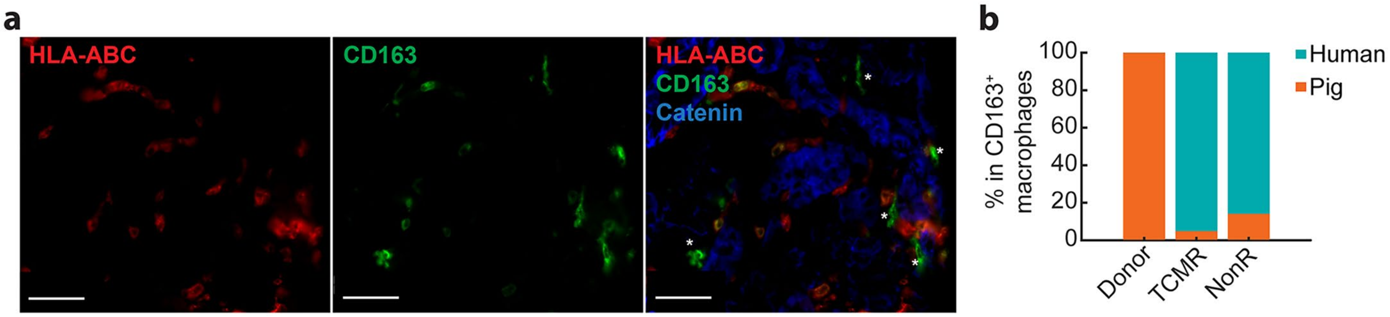

Extended Data Fig. 8 | Spatial localization and temporal quantification of porcine-derived CD163$^+$ macrophages in kidney xenograft biopsies. (**a**) Representative images of CD163, human HLA-ABC, and β-catenin staining in kidney biopsies of xenograft tissue on post-transplant day 8. Images were captured at the same location on the slide for each marker. HLA-ABC labels human MHC class I; CD163 labels M2 macrophages; β-catenin labels tubular epithelium. Tissue-resident pig macrophages (CD163$^+$ HLA-ABC$^-$) are indicated by an asterisk (*). Scale bar: 50 µm; (**b**) Quantification of the percentage of human (HLA-ABC$^+$) and porcine (HLA-ABC$^-$) cells among CD163$^+$ macrophages on whole-slide sections in kidney biopsies from donor, day 8 (TCMR), and day 34 (non-rejection, nonR) post-xenotransplant (see Methods for gating strategies). Quantification was independently repeated twice with similar results.

nature portfolio

Corresponding author(s): Leonardo Riella
Last updated by author(s): Sep 25, 2025

Reporting Summary

Nature Portfolio wishes to improve the reproducibility of the work that we publish. This form provides structure for consistency and transparency in reporting. For further information on Nature Portfolio policies, see our Editorial Policies and the Editorial Policy Checklist.

Statistics

For all statistical analyses, confirm that the following items are present in the figure legend, table legend, main text, or Methods section.

n/a	Confirmed	
☐	☒	The exact sample size (*n*) for each experimental group/condition, given as a discrete number and unit of measurement
☐	☒	A statement on whether measurements were taken from distinct samples or whether the same sample was measured repeatedly
☐	☒	The statistical test(s) used AND whether they are one- or two-sided *Only common tests should be described solely by name; describe more complex techniques in the Methods section.*
☐	☒	A description of all covariates tested
☐	☒	A description of any assumptions or corrections, such as tests of normality and adjustment for multiple comparisons
☐	☒	A full description of the statistical parameters including central tendency (e.g. means) or other basic estimates (e.g. regression coefficient) AND variation (e.g. standard deviation) or associated estimates of uncertainty (e.g. confidence intervals)
☒	☐	For null hypothesis testing, the test statistic (e.g. *F*, *t*, *r*) with confidence intervals, effect sizes, degrees of freedom and *P* value noted *Give P values as exact values whenever suitable.*
☒	☐	For Bayesian analysis, information on the choice of priors and Markov chain Monte Carlo settings
☒	☐	For hierarchical and complex designs, identification of the appropriate level for tests and full reporting of outcomes
☒	☐	Estimates of effect sizes (e.g. Cohen's *d*, Pearson's *r*), indicating how they were calculated

Our web collection on statistics for biologists contains articles on many of the points above.

Software and code

Policy information about availability of computer code

Data collection	10X Genomics Chromium System SOMAscan analysis (SomaLogic) FACSDiva software (BD Biosciences) Luminex200 system (Luminex) nCounter system (NanoString) Artemis software (Rarecyte) Q Exactive HF-X mass spectrometer system (Thermo Fisher Scientific)
Data analysis	pyroe 0.9.0 salmon 1.10.3 alevin 0.10.0 Seurat 5.1.0 harmony 1.2.0 Fastqc 0.12.0 Fastp 1.0.1 Tximport 1.32.0 sra-tools 2.10.7 MZmine 4.5 emzed FlowJo software 10.9.0 (BD Biosciences)

MATLAB (MathWorks)
scikit-learn 1.6.1
scikit-fda 0.9.1
numpy 2.2.0
matplotlib 3.8.0
networkx 3.4.2
GSEApy 1.1.7
netgraph 4.13.1
adjustText 1.3.0
IOBR 0.99.8
circlize package 0.4.16
R 4.4.2
Scipy 1.11.4
seaborn 0.13.2

For manuscripts utilizing custom algorithms or software that are central to the research but not yet described in published literature, software must be made available to editors and reviewers. We strongly encourage code deposition in a community repository (e.g. GitHub). See the Nature Portfolio guidelines for submitting code & software for further information.

Data

Policy information about availability of data

All manuscripts must include a data availability statement. This statement should provide the following information, where applicable:

- Accession codes, unique identifiers, or web links for publicly available datasets
- A description of any restrictions on data availability
- For clinical datasets or third party data, please ensure that the statement adheres to our policy

Quantification matrices for the resulting datasets (including PBMC single-cell RNA-seq, bulk RNA-seq, proteomics, and metabolomics) are available on Harvard Dataverse (doi: https://doi.org/10.7910/DVN/KGQITG)

Research involving human participants, their data, or biological material

Policy information about studies with human participants or human data. See also policy information about sex, gender (identity/presentation), and sexual orientation and race, ethnicity and racism.

Reporting on sex and gender	The patient’s sex was documented; however, analyses stratified by sex were not conducted because of the limited sample size.
Reporting on race, ethnicity, or other socially relevant groupings	Our study did not report race, ethnicity, or other socially relevant groupings.
Population characteristics	We reported sex, age and past relevant medical history of patient.
Recruitment	A patient was recruited among kidney transplantation candidates approved for transplant at MGH with ongoing challenges with dialysis, no potential living donor, and an expected waiting time for a deceased donor of longer than 4 years
Ethics oversight	The patient provided written informed consent, as approved by the MGH Human Research Committee (IRB no: 2023P003631).

Note that full information on the approval of the study protocol must also be provided in the manuscript.

Field-specific reporting

Please select the one below that is the best fit for your research. If you are not sure, read the appropriate sections before making your selection.

☒ Life sciences ☐ Behavioural & social sciences ☐ Ecological, evolutionary & environmental sciences

For a reference copy of the document with all sections, see nature.com/documents/nr-reporting-summary-flat.pdf

Life sciences study design

All studies must disclose on these points even when the disclosure is negative.

Sample size	We are reporting the first pig kidney xenotransplantation into a living human, n = 1
Data exclusions	Poor-quality nuclei and doublets were excluded from scRNA-seq datasets following established protocols, using consistent thresholds across all samples and datasets to maintain comparability. No data were excluded from the other analyses.
Replication	All data were obtained from a single patient and, as such, are not reproduced in this report. All reported clinical labs reflect individual sample

Replication

runs and are therefore not available in duplicate or triplicate. Immune surveillance assays performed as part of our analyses were performed in duplicate whens samples was not limited. The pathology images were determined through the analysis of multiple tissue sections, with representative images included in this report.

Randomization

No randomization was performed.

Blinding

ScRNAseq, proteomics, metabolomics, and bulk RNAseq analysis were performed by blinded operators. Samples were ran in simple batches to minimize technical variability.

Reporting for specific materials, systems and methods

We require information from authors about some types of materials, experimental systems and methods used in many studies. Here, indicate whether each material, system or method listed is relevant to your study. If you are not sure if a list item applies to your research, read the appropriate section before selecting a response.

Materials & experimental systems

n/a	Involved in the study	
☐	☒	Antibodies
☒	☐	Eukaryotic cell lines
☒	☐	Palaeontology and archaeology
☐	☒	Animals and other organisms
☐	☒	Clinical data
☒	☐	Dual use research of concern
☒	☐	Plants

Methods

n/a	Involved in the study	
☐	☐	ChIP-seq
☐	☒	Flow cytometry
☐	☐	MRI-based neuroimaging

Antibodies

Antibodies used

CD8 BUV737 1:20 SK1 BD Biosciences 612754
CD4 BUV395 1:20 SK3 BD Biosciences 563550
CD3 AF700 1:50 UCHT1 BioLegend 300424
CD19 PE-Cy5 1:20 SJ25C1 BioLegend 363042
CD127 PerCP-Cy5.5 1:20 A019D5 BioLegend 351322
CD25 PE-Cy7 1:20 BC96 BioLegend 302612
CCR7 PE-Dazzle 594 1:20 G043H7 BioLegend 353236
CD45RA APC 1:20 HI100 BioLegend 304112
CD56 BUV737 1:20 NCAM16.2 BD Biosciences 612766
HLA-DR BV650 1:20 L243 BioLegend 307650
CD14 BV510 1:50 M5E2 BioLegend 301842
CD11c AF700 1:20 3.9 BioLegend 301648
CD3 PerCP-Cy5.5 1:50 UCHT1 BioLegend 300430
CD19 PerCP-Cy5.5 1:50 HIB19 BioLegend 302230

AlexaFluor 520 CD45 Leukocyte D9M8I RareCyte 62-1001-501
ArgoFluor 548 NKG2A NK cell EPR23737-127 Abcam ab273516
ArgoFluor 602 CD163 Macrophage EDHu-1 Novus NB110-40686
ArgoFluor 624 CD8a T Cytotoxic AMC908 RareCyte 62-1007-601
ArgoFluor 706 CD4 T Helper EPR6855 RareCyte 62-1098-701
ArgoFluor 760 CD68 Macrophage D4B9C RareCyte 62-1013-701
ArgoFluor 784 Podocin Glomerulis Polyclonal Sigma-Aldrich P0372
ArgoFluor 845 β-catenin Tubule Epithelium D10A8 Cell Signaling 84441SF
FITC HLA-ABC Human HLA class I W6/32 Thermo Fisher 11-9983-41
ArgoFluor 698 CD31 Endothelium Polyclonal Novus NB100-2284

Validation

All antibodies were obtained from commercial sources. Manufacturer documentation was reviewed and antibodies were tested in PBMC or control slides prior to use.

Animals and other research organisms

Policy information about studies involving animals; ARRIVE guidelines recommended for reporting animal research, and Sex and Gender in Research

Laboratory animals

A Yucatan miniature pig was genetically engineered with 69 genomic modifications, including the deletion of three major glycan antigens, the overexpression of seven human transgenes (TNFAIP3, HMOX1, CD47, CD46, CD55, THBD, and EPCR), and the inactivation of porcine endogenous retroviruses. Further information can be found in Kawai et al., NEJM 2025.

Wild animals

The study did not involve wild animals.

Reporting on sex	We used a female pig. Further information is described in Kawai et al., NEJM 2025.
Field-collected samples	The study did not involve samples collect from the field
Ethics oversight	Biomere IACUC protocol 24-04.

Note that full information on the approval of the study protocol must also be provided in the manuscript.

Clinical data

Policy information about clinical studies

All manuscripts should comply with the ICMJE guidelines for publication of clinical research and a completed CONSORT checklist must be included with all submissions.

Clinical trial registration	Single patient IND # 30360
Study protocol	(IRB no: 2023P003631). Single patient IND # 30360
Data collection	Data collected from a single patient.
Outcomes	kidney function, graft survival, patient surivval

Plants

Seed stocks	N/A
Novel plant genotypes	N/A
Authentication	N/A

ChIP-seq

Data deposition

☐ Confirm that both raw and final processed data have been deposited in a public database such as GEO.

☐ Confirm that you have deposited or provided access to graph files (e.g. BED files) for the called peaks.

Data access links *May remain private before publication.*	N/A
Files in database submission	N/A
Genome browser session (e.g. UCSC)	N/A

Methodology

Replicates	N/A
Sequencing depth	N/A
Antibodies	N/A
Peak calling parameters	N/A
Data quality	N/A
Software	N/A

Flow Cytometry

Plots

Confirm that:

☒ The axis labels state the marker and fluorochrome used (e.g. CD4-FITC).

☒ The axis scales are clearly visible. Include numbers along axes only for bottom left plot of group (a 'group' is an analysis of identical markers).

☒ All plots are contour plots with outliers or pseudocolor plots.

☒ A numerical value for number of cells or percentage (with statistics) is provided.

Methodology

Sample preparation	Sections "Recipient PBMC and serum isolation", "Isolation of lymph node cells", and "Flow cytometry" of the Methods section
Instrument	LSR Fortessa X-20 flow cytometer (BD Biosciences)
Software	FACSDiva software (BD Biosciences)
Cell population abundance	We haven't performed sorting experiments
Gating strategy	Detailed in Supplementary Fig 2.

☒ Tick this box to confirm that a figure exemplifying the gating strategy is provided in the Supplementary Information.

Magnetic resonance imaging

Experimental design

Design type	N/A
Design specifications	N/A
Behavioral performance measures	N/A

Acquisition

Imaging type(s)	N/A
Field strength	N/A
Sequence & imaging parameters	N/A
Area of acquisition	*State whether a whole brain scan was used OR define the area of acquisition, describing how the region was determined.*

Diffusion MRI ☐ Used ☒ Not used

Preprocessing

Preprocessing software	N/A
Normalization	N/A
Normalization template	N/A
Noise and artifact removal	N/A
Volume censoring	*Define your software and/or method and criteria for volume censoring, and state the extent of such censoring.*

Statistical modeling & inference

Model type and settings	N/A
Effect(s) tested	N/A

Specify type of analysis: ☐ Whole brain ☐ ROI-based ☐ Both

Statistic type for inference (See Eklund et al. 2016)	*Specify voxel-wise or cluster-wise and report all relevant parameters for cluster-wise methods.*
Correction	N/A

Models & analysis

n/a	Involved in the study
☒	☐ Functional and/or effective connectivity
☒	☐ Graph analysis
☒	☐ Multivariate modeling or predictive analysis